bioRxiv preprint doi: https://doi.org/10.1101/2020.06.23.167130; this version posted June 24, 2020. The copyright holder for this preprint (which was not certified by peer review) is the author/funder, who has granted bioRxiv a license to display the preprint in perpetuity. It is made available under aCC-BY-NC-ND 4.0 International license.

Reduced nuclear lamin A/C enhances cancer cell squeezing through rigid barriers, does not facilitate endothelial crossing, and impairs experimental metastasis

Francesco Roncato[1], Ofer Regev[1], Sara W. Feigelson[1], Sandeep Kumar Yadav[1], Lukasz Kaczmarczyk[2], Nehora Levi[2], Diana Drago-Garcia[3], Samuel Ovadia[1], Marina Kizner[1], Yoseph Addadi[4], João Cruz Sabino[5], Yossi Ovadya[6], Sérgio Fernandes de Almeida[5], Ester Feldmesser[3], Gabi Gerlitz[2] and Ronen Alon[1,7,8]

1 Department of Immunology, Weizmann Institute of Science, Rehovot, 76100, Israel

2 Department of Molecular Biology, Ariel University, Kiryat Hamada, Ariel, 40700, Israel

3 Department of Biological Regulation, Weizmann Institute of Science, Rehovot 76100, Israel

4 Life Sciences Core Facilities, Weizmann Institute of Science, Rehovot, 76100, Israel

5 Instituto de Medicina Molecular João Lobo Antunes, Faculdade de Medicina, Universidade de Lisboa, Lisboa, 1649-028, Portugal.

6 Department of Molecular Cell Biology, Weizmann Institute of Science, 76100 Rehovot, Israel

7 Corresponding author

8 Lead Contact

bioRxiv preprint doi: https://doi.org/10.1101/2020.06.23.167130; this version posted June 24, 2020. The copyright holder for this preprint (which was not certified by peer review) is the author/funder, who has granted bioRxiv a license to display the preprint in perpetuity. It is made available under aCC-BY-NC-ND 4.0 International license.

Summary

The mechanisms by which the nuclear lamina of tumor cells control their migration and survival are poorly understood. Lamin A and its splice variant lamin C are key nuclear lamina proteins that control nucleus stiffness and chromatin conformation. Genetically reduced lamin A/C levels in two metastatic murine cancer lines, B16F10 melanoma and E0771 breast carcinoma, facilitated cell squeezing through rigid pores, elevated nuclear deformability, reduced H3K9Me3 heterochromatin, and altered gene transcription. Nevertheless, the transendothelial migration capacity of lamin A/C low cells both in vitro and in vivo, through lung capillaries, remained normal. Cancer cell growth within orthotopic implants and DNA damage-induced growth arrest were also insensitive to downregulated lamin A/C expression. Experimental lung metastasis of lamin A/C low cancer cells, however, was markedly reduced. Taken together, our results suggest that reduced lamin A/C expression increases nuclear squeezing through rigid confinements, does not impact intrinsic cancer cell growth and migration, but impairs metastatic survival in lungs.

bioRxiv preprint doi: https://doi.org/10.1101/2020.06.23.167130; this version posted June 24, 2020. The copyright holder for this preprint (which was not certified by peer review) is the author/funder, who has granted bioRxiv a license to display the preprint in perpetuity. It is made available under aCC-BY-NC-ND 4.0 International license.

Introduction

The nucleus is the largest and stiffest organelle in all cells and therefore imposes the main barrier for cell crossing of cellular and mechanically resistant extracellular barriers (Burke and Stewart, 2013; Friedl et al., 2011; Fruleux and Hawkins, 2016). The nucleus must undergo various shape changes during cell migration through cellular and extracellular barriers (Friedl et al., 2011). Lamin A and its splice variant lamin C are key nuclear lamina intermediate filament proteins that control nucleus stiffness (Burke and Stewart, 2013; Lammerding et al., 2006; Roman et al., 2017; Shin et al., 2013), and regulate chromatin conformation and accessibility (Bronshtein et al., 2015; Towbin et al., 2009). A-type lamins also control nuclear crosstalk with all types of the cell cytoskeleton, including microtubules and actin filaments (Chambliss et al., 2013; Chang et al., 2013; Etienne-Manneville and Lammerding, 2017; Khatau et al., 2009; Lombardi and Lammerding, 2011) and thereby regulate nuclear location and response to mechanical signals from the extracellular environment (Borrego-Pinto et al., 2012; Gonzalez-Granado et al., 2014; Graham et al., 2018; Kim and Wirtz, 2015; Kirby and Lammerding, 2018; Swift et al., 2013).

Alterations in nuclear lamina stiffness can take place by various DNA damaging processes including the recently described nuclear autophagy, nucleophagy (Dou et al., 2015) or by genetic changes (Broers and Ramaekers, 2014). The latter changes can be experimentally introduced by controlled suppression or overexpression of lamin A/C and such changes have been studied in different types of cells migrating through variably rigid confinements in vitro and in vivo (Denais et al., 2016). The soft nuclei of most leukocytes contain low levels of lamin A/C and high levels of other lamins, primarily of the B type (Shin et al., 2013). The low ratio of A and B lamins allows leukocytes to undergo massive and rapid deformation during fast squeezing through vascular endothelial junctions and collagenous interstitial spaces (Yadav et al., 2018). How nuclear squeezing is regulated in solid cancer cells migrating through variable interstitial ECM barriers and constricted vascular spaces is only partially understood (Denais et al., 2016; Raab et al., 2016; Wolf et al., 2013). In contrast to leukocyte nuclei which express very low levels of lamins A/C, the nuclei of variably invasive metastatic tumor cells of mesenchymal origin contain high levels of these lamins and are therefore generally more stiff, imposing major restrictions on the ability of these cells to cross endothelial junctions and interstitial barriers (Cao et al., 2016). Unlike fibrillar collagens in most interstitial spaces, the cytoskeleton of endothelial cells which comprise the major barriers for nuclear squeezing is fairly elastic and contractile (Barzilai et al., 2017; Heemskerk et al., 2016). In contrast, collagenous barriers cannot undergo such extensive remodeling and so the relatively stiff nuclei of solid tumor cells might not efficiently cope with these rigid barriers (Yadav et al., 2018). Support for this idea was

bioRxiv preprint doi: https://doi.org/10.1101/2020.06.23.167130; this version posted June 24, 2020. The copyright holder for this preprint (which was not certified by peer review) is the author/funder, who has granted bioRxiv a license to display the preprint in perpetuity. It is made available under aCC-BY-NC-ND 4.0 International license.

recently provided by experiments with leukocytes overexpressing lamin A: a 10-fold increase in the ratio of lamin A to lamin B dramatically restricted leukocyte nuclear squeezing through rigid pores and dense collagenous barriers but was largely permissive for leukocyte transendothelial migration (Yadav et al., 2018).

Lamins A/C are also involved in chromatin conformation and epigenetics via their interactions with heterochromatin, transcriptionally repressed tightly folded chromatin tethered to the nuclear lamina (Becker et al., 2016; Dechat et al., 2010; Harr et al., 2015). Nevertheless, the direct contributions of lamins to cancer cell migration, growth, and malignancy have been in debate (Broers and Ramaekers, 2014). On one hand, lamin A/C expression is reduced in several solid cancers (Bell and Lammerding, 2016; Denais and Lammerding, 2014; Kaufmann et al., 1991), both lamins are absent in around 40% of human breast cancer tissues (Capo-chichi et al., 2011), and reduced lamin A/C expression is a sign of poor prognosis in skin, breast, lung and colon cancers (Broers et al., 1993; Capo-chichi et al., 2011; Venables et al., 2001). On the other hand, overexpression of A-type lamins in some cancer cells causes enhanced growth, invasion, and migration by activation of the PI3K/AKT/PTEN pathway (Kong et al., 2012). Part of these discrepancies are attributed to the complex roles of A-type lamins in protecting the nuclei from mechanical nuclear rupture, DNA damage, and cell growth arrest (Cho et al., 2019). These discrepancies have motivated us to address these standing questions by controlled downregulation of lamin A/C expression introduced into bona fide metastatic cells. We speculated that extravasation of circulating cancer cells from different blood vessels, and in particular from the relatively impermeable lung capillaries, are favored by the softening of tumor cell nuclei via downregulation of lamin A/C. We chose to systematically address in vitro and in vivo in syngeneic mice models if and how downregulation of lamins A/C expression with retained levels of B lamins alters invasive and proliferative properties of prototypic metastatic cell lines, namely, B16 melanoma and E0771 breast carcinoma. In vitro, downregulated lamin A/C levels introduced by ectopic expression of lamin A/C specific shRNA dramatically facilitated the squeezing of both cells through rigid pores, reduced its heterochromatin content, and altered its transcriptional signature. Surprisingly, however, upon adoptive transfer, lamin A/C deficient cells normally crossed the pulmonary circulation and their early survival inside the lung parenchyma was insensitive to loss of lamin A/C. Furthermore, the dramatic mechanical and epigenetic alterations imposed by lamin A/C downregulation did not affect tumor cell proliferation and susceptibility to DNA stress in vitro, and did not affect tumor growth in primary orthotopic tumors. Nevertheless, the ability of lamin A/C low melanoma and breast cancer cells to survive and generate metastatic lesions in the lungs was markedly compromised. Our results collectively suggest that melanoma and breast cancer cells, like leukocytes, can squeeze their nuclei through endothelial barriers

bioRxiv preprint doi: https://doi.org/10.1101/2020.06.23.167130; this version posted June 24, 2020. The copyright holder for this preprint (which was not certified by peer review) is the author/funder, who has granted bioRxiv a license to display the preprint in perpetuity. It is made available under aCC-BY-NC-ND 4.0 International license.

independently of their relative nuclear lamin A/C content. Furthermore, high content of lamin A/C does not seem to protect cancer cell nuclei from cell death intrinsically in their tissue of origin in vivo but does allow these cells to grow more efficiently in a foreign organ of metastasis.

Results

A new setup for analysis of cytoskeletal regulated nucleus deformation in tumor cells undergoing transendothelial migration

Cancer metastasis into lungs occurs nearly exclusively through the pulmonary capillaries (Miles et al., 2008). The main mechanical obstacle to the extravasation of solid tumor cells entrapped inside capillaries and other microvessels is their stiff nuclei (Davidson et al., 2014; Friedl et al., 2011). To assess how changes in the composition and deformability of the tumor nucleus promotes tumor cell squeezing and TEM, we first established a new in vitro video-microscopy based assay in which nuclear squeezing of tumor cell crossing confluent monolayers of bEnd.3 murine endothelial cells can be compared. Nucleus location, deformation and squeezing in individual transmigrating tumor cells could be readily tracked in real time by fluorescence and phase contrast microscopy of tumor cells whose nuclei was prelabeled with the nuclear dye Hoechst (Figure 1A; Movie S1). This assay allowed us to follow how individual tumor cells complete an entire sequence of TEM steps immediately after settling upon confluent endothelial monolayers, including protrusion, generation of large sub-endothelial pseudopodia (lamellipodia), squeezing their nuclei, tail detachment, and locomotion underneath the endothelial monolayer (Figure 1A; Movie S1). This assay also allowed us to distinguish between these transmigrating tumor cells and tumor cells that failed to complete TEM either because of their inability to squeeze their nuclei (Figure 1B, SEP category), protrude (Figure 1B, SA category), or adhere and spread on the apical endothelial surface (Figure 1B, Round category). Notably, we did not observe any other alternative readout of TEM, such as a reported intercalation of individual tumor cells in between ECs without a final squeezing of the tumor nuclei underneath the endothelial monolayer (Reymond et al., 2012) (Figures 1A and 1B). Furthermore, out of three murine cancer cell lines tested in this new assay, namely B16F10, E0771, and LL/2, B16 melanoma exhibited the highest extent of TEM (Figure 1C). Reminiscent of leukocyte TEM, all three tumor cells crossed the endothelial monolayer through paracellular junctions, but none of these tumor cells could attach to the endothelial monolayers under physiological or sub-physiological shear stresses (data not shown). Since tumor cell emigration from the lung vasculature occurs predominately via physical entrapment inside capillaries (Reymond et al., 2013), tumor cell emigration across the endothelial lining of these vessels does not require

bioRxiv preprint doi: https://doi.org/10.1101/2020.06.23.167130; this version posted June 24, 2020. The copyright holder for this preprint (which was not certified by peer review) is the author/funder, who has granted bioRxiv a license to display the preprint in perpetuity. It is made available under aCC-BY-NC-ND 4.0 International license.

the pre-attachment of tumor cells to endothelial cells under flow. Therefore, our tumor TEM assay was performed under shear-free conditions. Notably, melanoma TEM did not depend on endothelial stimulation with inflammatory cytokines (data not shown), a prerequisite for neutrophil and T cell TEM (Shulman and Alon, 2012). The contribution of prototypic cancer cell attractants to this melanoma TEM readout, including CXCL12, VEGF-A and EGF was also ruled out, because B16F10 melanoma cells migrated towards the c-Met ligand HGF but failed to migrate towards these attractants (Figure S1A). Melanoma B16F10 TEM in vitro was also independent of c-Met (Figures S1B and S1C) or of either tumor or endothelial expressed MMPs (Figure S1D). Interestingly, in spite of the high β1 and β3 integrin expression levels of these melanoma cells (Figure 1D) and their function in B16 chemotaxis (Figure S2A) and spreading on endothelial deposited extracellular matrix (ECM) (Figure S2B), the ability of B16 cells to protrude, establish a leading edge on the endothelial basement membrane ECM, squeeze, and displace the endothelial monolayer from its basement membrane took place independently of functional tumor β1 and β3 integrins (Figure 1E). Taken together, the ability of metastatic B16 melanoma cells to cross endothelial monolayers in vitro does not depend on the ability of their integrins to interact with extracellular matrix components of the endothelial deposited basement membrane and does not involve tumor or endothelial MMP proteolytic activity.

Leukocyte TEM is an extremely rapid process initiated by chemokine-triggered protrusion, formation of a sub-endothelial leading edge, and acto-myosin-driven nuclear deformation associated with formation of nuclear lobes which get rapidly translocated into the sub-endothelial leukocyte-pseudopodia (Barzilai et al., 2017; Yadav et al., 2018). Notably, the TEM of all 3 types of cancer cells visualized in our system was over 30-fold slower due to a very slow formation of the sub-endothelial leading edge (t= 26±22 min for B16F10 as compared to 30±15 s for T cells (Barzilai et al., 2017)) and to the inability of the tumor nucleus to translocate into this leading edge as it is generated, a characteristic of leukocyte TEM (Movie S3) (Barzilai et al., 2017; Yadav et al., 2018).

To further delineate the basis for these striking differences, we next assessed the roles of the actin and microtubule (MT) cytoskeletons in individual steps of B16 melanoma TEM in our in vitro system. As expected, B16F10 TEM was completely abolished by pretreatment with the actin drug jasplakinolide that blocks actin turnover. This drug completely eliminated initial B16F10 spreading on the endothelial monolayer (Figure 1F), and B16 spreading on the endothelial-deposited basement membrane (Figure 1G). Jasplakinolide also blocked both chemotactic and haptotactic melanoma migration through pores (Figures 1H and 1I). In contrast, interference with MT turnover with zampanolide, a taxol-like inhibitor of microtubule disassembly (Field et al., 2012) did not abrogate B16

bioRxiv preprint doi: https://doi.org/10.1101/2020.06.23.167130; this version posted June 24, 2020. The copyright holder for this preprint (which was not certified by peer review) is the author/funder, who has granted bioRxiv a license to display the preprint in perpetuity. It is made available under aCC-BY-NC-ND 4.0 International license.

spreading on the endothelial deposited basement membrane (Figure 1G; Movie S4). Blocking melanoma cell MT turnover partially reduced, however, initial melanoma spreading (Figure 1F, round category), and reduced B16 cell protrusion through endothelial junctions (Figure 1F, SEP category). Blocking MT turnover also dramatically suppressed the ability of melanoma cells to squeeze their nuclei through endothelial junctions and complete TEM (Figure 1F, TEM category). In contrast to melanoma, blocking the MT turnover in T cells with the same drug only mildly interfered with their adhesion, protrusion, nuclear squeezing and TEM capacities (Figure S3A). Interference with the MT turnover of T cells also did not affect their chemotactic transmigration through pores (Figure S3B). Taken together, tumor cell TEM, in sharp contrast to leukocyte TEM (Barzilai et al., 2017; Yadav et al., 2019), involves an actin-based protrusion through the endothelial monolayer followed by a slow microtubule-mediated nuclear translocation into this tumor protrusion and tumor squeezing through the endothelial junction.

Lamin A downregulation in B16F10 cells increases nucleus deformability and squeezing through rigid pores but does not affect tumor transendothelial migration

To gain more insight into the ability of solid tumor cells to translocate their nuclei across endothelial junctions, we next downregulated lamin A and lamin C expression in the nuclei of the B16F10 melanoma cells by stably introducing into these tumor cells a lamin A/C shRNA construct targeting exon 8 of the *Lmna* gene (Figures 2A and 2B). The low deformability of the nuclei of solid tumor cells is attributed to high mechanical stiffness of their nuclear lamina. Since the nuclear lamina stiffness is sensitive to the ratio between type A lamins and type B lamins in both mesenchymal and hematopoietic cells (Shin et al., 2013), we expected that lamin A/C downregulation would increase nuclear deformability and squeezing capacities in our melanoma cell model. Downregulating lamin A and lamin C expression in the B16 melanoma line by 90%, but leaving lamin B1 levels intact, altered the ratio of type A to type B lamins by approximately 10-fold (Figure 2A). This lamin A/C downregulation resulted in a dramatic enhancement of B16 squeezing through small rigid pores but much less so through large pores (Figures 2C and 2D). A similar gain of squeezing of lamin A/C downregulated B16F10 cells was observed by transient *Lmna* gene exon-4 targeted siRNA mediated downregulation of lamin A/C transcription (Figure S4).

We next assessed if the dramatic effects of lamin A/C downregulation on B16F10 cell squeezing through rigid confinements also affected the ability of the nuclei of these tumor cells to squeeze in between and underneath the endothelial cells that comprise the endothelial barrier on their way to complete TEM. Strikingly, and in contrast to the squeezing results across rigid pores (Figures 2C and 2D), the extent of B16F10 TEM was not increased by lamin A/C downregulation (Figures 3A and 3B; Movie S5). However, the

bioRxiv preprint doi: https://doi.org/10.1101/2020.06.23.167130; this version posted June 24, 2020. The copyright holder for this preprint (which was not certified by peer review) is the author/funder, who has granted bioRxiv a license to display the preprint in perpetuity. It is made available under aCC-BY-NC-ND 4.0 International license.

extent of nuclear deformation for lamin A/C downregulated nuclei was significantly greater than that of the control tumor cells (Figure 3C). The nuclei of the lamin A/C deficient B16F10 also appeared more deformable when these cells were allowed to spread on a non-confined 2D substrate coated with the basement membrane deposited by the endothelial monolayer, although the motility of these cells remained normal (Figure 3D; Movie S6). These results collectively suggest that the reduced nuclear stiffness evident from the dramatically increased squeezing ability of lamin A/C deficient B16 through small rigid pores (Figures 2C and 2D) and the increased nuclear deformability of lamin A/C deficient B16F10 cells (Figures 3C and 3D) do not provide a migratory advantage for the transmigration of these cells through endothelial barriers. These results suggest that the high mechanical flexibility of the endothelial cytoskeletal barriers maintained by their rapid actin turnover (Ofer et al., 2011) and their contractility (Heemskerk et al., 2016) overrides the poor squeezing capacity of lamin A/C rich nuclei through rigid barriers.

Lamin A downregulation does not increase B16F10 extravasation across lung vessels in vivo and does not accelerate melanoma apoptosis in the lung parenchyma

Our in vitro results thus indicated that lamin A/C downregulation in tumor cells enhance their squeezing through rigid confinement without affecting the ability of these cells to transmigrate across endothelial barriers. The main mechanical obstacle for the extravasation of solid cancer cells across blood vessels in vivo is their stiff nuclei (Shin et al., 2013). To assess the distinct migratory outcomes of lamin A/C downregulation in the B16 melanoma cells in vivo, we introduced an experimental lung metastasis model based on i.v. injection of minute numbers of fluorescently labeled B16F10 (Figure S5), in order to minimize non-physiological inflammatory responses associated with a bolus of cancer cells that simultaneously enter the lung vasculature. Tumor metastasis into lung occur nearly exclusively through the pulmonary capillaries (Miles et al., 2008), an extensive network of relatively impermeable capillaries (Chambers et al., 2002) considered to be poorly permeable compared with vessels targeted by metastatic cells at other organs like the bone marrow and liver (Valastyan and Weinberg, 2011). I.V. injections of tumor cells are extensively used for studying hematogenous dissemination and expansion in the lung (Gorelik and Flavell, 2001). Since the tumor cells are introduced i.v. in a single event, their arrival at the lung vasculature is synchronized which allows accurate temporal dissection of the earliest extravasation steps taken by individual circulating metastatic cells entering the lung vasculature several hours post injection. To determine the effects of lamin A/C downregulation on earliest tumor cell extravasation across the lung capillaries, we compared the cancer cell partition inside and outside lung vessels with newly developed 3D imaging of the injected fluorescently labeled cancer cells in relation to CD31 stained lung vessels

bioRxiv preprint doi: https://doi.org/10.1101/2020.06.23.167130; this version posted June 24, 2020. The copyright holder for this preprint (which was not certified by peer review) is the author/funder, who has granted bioRxiv a license to display the preprint in perpetuity. It is made available under aCC-BY-NC-ND 4.0 International license.

(Figures 4A and 4B; Movie S7). Strikingly, lamin A/C downregulated B16F10 cells extravasated at similar efficiencies to normal B16F10 cells (Figure 4C: Movies S8, S9 and S10). Lamin A/C downregulation also did not affect the total number of B16F10 cells accumulated inside the recipient lung at this early time points (Figure 4D). These results suggest that unlike its dramatic effects on tumor squeezing in vitro, but consistent with our TEM results in vitro (Figure 3A), lamin A/C suppression does not facilitate melanoma extravasation across lung vessels in vivo.

Reduced lamin A levels were reported to be proapoptotic to cells experiencing high mechanical stresses (Capo-chichi et al., 2011; Denais et al., 2016; Irianto et al., 2017; Raab et al., 2016). We therefore followed the post extravasation survival of the various cellular groups inside recipient lungs up to 72 h post i.v. injection by determining the recovery of live fluorescently labeled B16 cells from total cell suspensions of harvested lungs. Soon after entry to lung, B16F10 cells underwent massive death with only 10% of cells originally accumulated in the lung surviving in this organ 72 h later (Figure 4D). Notably, however, the number of B16F10 cells recovered was unaffected by lamin A/C downregulation (Figure 4D) indicating that early after entering into the lung parenchyma, lamin A/C deficient B16F10 do not become more prone to apoptosis, as would be expected were there higher susceptibility of their nuclei to mechanical rupture.

Lamin A/C downregulation reduces the content of H3K9Me3 heterochromatin and results in transcriptional changes

Lamin A/C KO was shown to reduce the major marker of constitutive heterochromatin H3K9me3 and the methyltransferases that generate it in primary cells (Liu et al., 2013). As predicted, lamin A/C downregulation led to lower levels of H3K9Me3 and significantly reduced levels of SUV39H2 and SETDB1, two main histone methyltransferases that maintain this suppressive epigenetic marker (Figures 5A and 5B). In contrast, facultative heterochromatin levels probed by the H3K27me3 marker remained unchanged (Figure 5B). This global H3K9me3 reduction was not associated with global repression of transcription as determined by a transcription run-on experiment (Figure 5C). Notably, transcription of specific genes may be altered by reduced H3K9me3 levels and lamin A/C deficiency was reported to increase chromatin dynamics, which could also affect transcription (Bronshtein et al., 2015; Solovei et al., 2013; Sullivan et al., 1999). To evaluate these possibilities, we performed RNA-seq analysis on control and lamin A/C shRNA transduced B16F10 cells. We found that the transcript levels of LINC complex components such as nesprins 1-4, emerin, as well as of other lamin A/C interactors involved in heterochromatin content and stability (e.g. ,Trim28, Tpr or Nup153 (Krull et al., 2010; Kubben et al., 2010)) were all normally transcribed in lamin A/C deficient B16 cells (Table S1). Lamin A/C downregulated B16F10

bioRxiv preprint doi: https://doi.org/10.1101/2020.06.23.167130; this version posted June 24, 2020. The copyright holder for this preprint (which was not certified by peer review) is the author/funder, who has granted bioRxiv a license to display the preprint in perpetuity. It is made available under aCC-BY-NC-ND 4.0 International license.

cells exhibited, however, major downregulation in several hundred genes, including nuclear matrix genes, nuclear body genes, as well as in lamin B receptor (Figures 5D, 5E and S6; Table S1). Consistent with their similar transmigration properties in vitro and similar capacity to extravasate lung capillaries in vivo, our transcript analysis did not indicate any differences in vascular permeability factors such as VEGF family member levels, MMP levels, or canonical cytoskeletal machineries (e.g., Rho GTPases, myosins)(Table S1).

Lamin A/C downregulation does not accelerate cell proliferation, tumor growth in vivo, or lung micrometastasis

Our transcriptional analysis did not detect changes in genes which are predicted to affect melanoma growth (Table S1). To directly assess the outcomes of the reduced chromatin repression changes induced by lamin A/C on the proliferative properties of B16 melanoma cells, we next analyzed the proliferation of control and lamin A/C shRNA transduced B16F10 cells in vitro. Although melanoma cells deficient in lamin A/C expression exhibited slightly higher growth rates in culture, daily replacement of the culture medium resulted in identical rates of in vitro proliferation (Figures 6A and 6B), suggesting the lamin A/C deficient cells may secrete some proliferation stimulating factors. Furthermore, when the lamin A/C low B16F10 cells or their control counterparts were subcutaneously implanted (at 10-20 fold lower numbers than in commonly used orthotopic melanoma models in order to avoid the masking of any potential growth differences), their growth in vivo remained similar (Figure 6C). Histological analysis of the orthotopic tumors also failed to show any noticeable differences in the vascular microenvironment of these implanted tumors (data not shown). Finally, the ability of individual B16F10 cells accumulated inside the lung parenchyma to generate metastatic lesions was significantly reduced by lamin A/C downregulation (Figure 6D).

We next reasoned that reduced lamin A/C content might render the nuclei of our model melanoma cells more susceptible to DNA damage. Interestingly, lamin A/C deficient B16 cells remained as resistant as control melanoma cells to apoptosis and growth arrest induced by the DNA damaging and cell cycle arrest reagent etoposide during the first 72 hours of treatment (Dai et al., 2017) (Figures 6E and S7). However, after an additional incubation period without etoposide, a higher fraction of the lamin A/C deficient B16 cells than of control B16 cells was driven into senescence (Figure 6F). This result is consistent with a report that implicates lamin A/C in DNA repair (Maynard et al., 2019). Taken together, our findings suggest that lamin A/C deficiency can modestly increase melanoma susceptibility to chemically induced DNA stress but does not affect melanoma growth in vitro or in vivo.

bioRxiv preprint doi: https://doi.org/10.1101/2020.06.23.167130; this version posted June 24, 2020. The copyright holder for this preprint (which was not certified by peer review) is the author/funder, who has granted bioRxiv a license to display the preprint in perpetuity. It is made available under aCC-BY-NC-ND 4.0 International license.

Reduced lamin A/C levels in the E0771 breast cancer cell line recapitulate the in vitro and in vivo properties of lamin A/C deficient B16 melanoma cells

We next reasoned that reduced lamin A/C levels could differentially impact distinct types of cancer cells. We therefore addressed how reduced lamin A/C expression introduced into the bona fide breast cancer cells, the E0771 line, affect their squeezing, migration, epigenetics and growth properties both in vitro and in vivo. Genetically introduced downregulation of lamin A/C levels with conserved lamin B content (Figures 7A and S8A) dramatically facilitated cancer cell squeezing through rigid pores in vitro (Figures 7B and S8B), in agreement with our findings with B16F10 cells. While the nuclear circularity index of control E0771 cells was higher than that of control B16F10 cells (Figures 3D and S8C), the nuclei of these cells underwent significant increases in deformability (i.e. reduced circularity) upon lamin A/C downregulation (Figure S8C), reminiscent of the effect of lamin A/C downregulation on B16 nuclei (Figure 3D). Nevertheless, the transendothelial migration capacity of these cells in vitro and in vivo was insensitive to reduced lamin A/C expression (Figures 7C, S9A and S9B). Although downregulated lamin A/C expression resulted in reduced H3K9Me3 heterochromatin content and resulted in significant transcriptional changes (Figures 7D, 7E, S10A and S10B) it did not increase overall transcription rates (Figure S10C). Furthermore, primary breast cancer growth in vitro or in vivo in the mammary fat pad was also unaffected by lamin A/C downregulation (Figures 7F, 7G and S11A). DNA damage-induced growth arrest was also insensitive to downregulated lamin A/C expression (Figure 7H). Lamin A/C deficient E0771 cells also normally accumulated in recipient lungs when intravenously introduced into syngeneic recipient mice (Figure S11B). Nevertheless, breast cancer cells with low lamin A/C content failed to generate any metastatic lesions in the lungs (Figures 7I and 7J). Thus, although reduced nuclear content of lamin A/C does not impair breast cancer growth in the primary tissue and does not alter breast cancer cell extravasation from lung vessels into the lung parenchyma, it dramatically compromises the metastatic potential of these breast cancer cells in this organ, reminiscent of our observations with lamin A/C deficient melanoma cells.

Discussion

The nucleus is the most bulky organelle in all cells and is protected by a mechanically stable network underlying the inner nuclear membrane termed the nuclear lamina (Swift et al., 2013; Wilson and Foisner, 2010; Wolf et al., 2013). The nuclear lamina is thought to affect the shape and the mechanical properties of the nucleus, hence to control cell squeezing through different barriers (Rowat et al., 2013; Wolf et al., 2013; Yadav et al., 2018). The lamina also plays an important role in the maintenance of the nuclear envelope integrity as well as in the organization of the nucleus as a whole (Friedl et al., 2011; Kirby and

bioRxiv preprint doi: https://doi.org/10.1101/2020.06.23.167130; this version posted June 24, 2020. The copyright holder for this preprint (which was not certified by peer review) is the author/funder, who has granted bioRxiv a license to display the preprint in perpetuity. It is made available under aCC-BY-NC-ND 4.0 International license.

Lammerding, 2018). The nuclear lamina is also connected to highly condensed chromatin regions (heterochromatin) (Stephens et al., 2012; Wilson and Berk, 2010) and can affect chromatin conformation, and epigenetics (Fernández-Morera et al., 2010; Sullivan et al., 1999). The lamina also controls the entry of key growth control transcriptional factors including the mechanosensitive transcriptional activator YAP (Elosegui-Artola et al., 2017). Lamin A/C expression is reduced in several solid cancers but not others, and so the molecular basis of these changes and their direct link to cancer cell migration, survival and expansion have been under debate due to the complexity and diversity of tumor growth, survival, migration and metastasis (Harada et al., 2014; Kong et al., 2012).

We chose to address this standing question with two prototypic BL/6 metastatic cell lines, B16F10 melanoma and E0771 breast carcinoma. Taking both in vitro and in vivo reductionist approaches in syngeneic immunocompetent mice, we have systematically assessed how controlled suppression of the two type A lamins affects the specific growth and migratory properties of these cells under distinct physiologically relevant conditions and environmental challenges. Our in vitro findings of enhanced migration capabilities of the lamin A deficient cells in the transwell assay are in full agreement with previous results on the critical role of lamin A/C in the ability of cells of different origins to squeeze through rigid confinements in vitro (Aureille et al., 2017; Rowat et al., 2013). However, these deformability changes had no impact on the overall nuclear squeezing kinetics through endothelial junctions and under the endothelial monolayer, further indicating that endothelial barriers are highly permissive for nuclear passage (Barzilai et al., 2017) and well adapted to accommodate the squeezing of cells with bulky and stiff nuclei. The exceptionally slow rates of tumor transendothelial migration, compared to leukocytes, may provide the endothelial cytoskeleton with sufficient time to undergo remodeling including activation of contractility machineries to facilitate the squeezing of the relatively stiff nuclei of most tumor cells though junctions or transcellular pores (Khuon et al., 2010; Yadav et al., 2018). Our current study and other reports collectively suggest that the ability of the tumor cells to degrade in vivo glycoprotein and proteoglycan components of the perivascular and interstitial collagenous barriers may be rate limiting for their in vivo migration and thus more critical than their nuclear deformability (Bishop et al., 2007). In line with our current study, we previously found that when leukocyte nuclei were rendered artificially non-deformable by a 10-fold increase in their lamin A/C content, leukocyte squeezing through small rigid pores and chemokine-triggered crossing of thick collagen I barriers were dramatically restricted, with negligible effects on chemokine-dependent transendothelial migration capacity (Yadav et al., 2018). Thus, the squeezing ability of a given cell through rigid pores towards a chemotactic or a haptotactic signal assessed in vitro does not directly predict the interstitial migration capacity and endothelial crossing potential of that cell in vitro or in vivo.

bioRxiv preprint doi: https://doi.org/10.1101/2020.06.23.167130; this version posted June 24, 2020. The copyright holder for this preprint (which was not certified by peer review) is the author/funder, who has granted bioRxiv a license to display the preprint in perpetuity. It is made available under aCC-BY-NC-ND 4.0 International license.

In order to validate our in vitro TEM results, we developed a new experimental lung metastasis model to assess in vivo the intrinsic ability of our lamin A/C suppressed tumor cells to squeeze through the lung vasculature. Tumor metastasis into lungs occurs nearly exclusively through the pulmonary capillaries (Miles et al., 2008), an extensive network of relatively impermeable capillaries (Chambers et al., 2002) considered to be poorly permeable compared with vessels targeted by metastatic cells at other organs like the bone marrow and liver (Valastyan and Weinberg, 2011). By introducing a new method to accurately measure the relative efficiency of cancer cell emigration through these vessels, we found that highly invasive cells like melanoma B16 crossed these barriers in vivo independently of their lamin A/C content and irrespectively of their intrinsic nucleus deformability properties. Although poorly invasive, the ability of E0771 cells to cross identical pulmonary vascular barriers was also irrespective of their intrinsic nucleus deformability and lamin A/C content. Our in vivo results were also consistent with the transmigratory properties of these cells determined in our in vitro setups and suggest that the mechanical barrier imposed by lung capillaries for tumor nuclear passage is similar to that imposed by our experimental endothelial monolayers in vitro setups.

Metastasis involves not only cancer cell extravasation but also intravasation into tumor engulfed blood vessels (Joyce and Pollard, 2009). Although the extravasation capacity of a given cancer cell does not predict its intravasation potential across the tumor associated blood vessels at its original site of dissemination, both our in vitro and in vivo analysis of tumor cell squeezing through different endothelial barriers predict that tumor cell squeezing through endothelial junctions is not affected by lamin A/C downregulation. Furthermore, since the lung capillaries, where the majority of our cancer cell diapedesis took place, are less permeable than tumor associated vessels and were permissive for the squeezing of lamin A/C rich nuclei, it is likely that the leaky vessels surrounding the primary tumors also do not pose a barrier for melanoma or breast cancer intravasation. Likewise, melanoma and breast cancer crossing of lymphatic vessels nearby tumors, considered highly permeable cell barriers (Dyer and Patterson, 2010), is probably insensitive to the lamin A/C content of the tumor nuclei.

Our epigenetic analysis revealed lower levels of the constitutive heterochromatin marker H3K9me3 and the methyltransferases that generate it in lamin A/C deficient B16F10 and E0771 cells, consistent with previous reports on lamin A/C KO MEFs (Liu et al., 2013) and human fibroblasts expressing mutated type A lamins (Scaffidi and Misteli, 2006). Reduced heterochromatin content has been argued to reduce chromatin compaction in B16 melanoma and thereby restrict cell motility (Maizels et al., 2017). The increased squeezing rate of the lamin A/C deficient B16 cells and E0771 cells that we find in spite of their lower H3K9me3 content sheds new light on these earlier findings. Our data therefore suggest that

bioRxiv preprint doi: https://doi.org/10.1101/2020.06.23.167130; this version posted June 24, 2020. The copyright holder for this preprint (which was not certified by peer review) is the author/funder, who has granted bioRxiv a license to display the preprint in perpetuity. It is made available under aCC-BY-NC-ND 4.0 International license.

the altered mechanical properties in our melanoma and breast cancer cell models introduced by lamin A/C downregulation override any inhibitory effects of reduced heterochromatin content on chromatin compaction and cell motility (Maizels et al., 2017).

Alongside the heterochromatin changes associated with the reduced lamin A/C content of our B16F10 cells, we could detect significant changes in the RNA levels of over 290 genes. Major affected transcriptional pathways in these cells involved nuclear matrix genes and RNA processing genes rather than genes involved in cell motility. Reduced lamin A/C content in the E0771 cells, resulted, however, in different transcriptional outcomes. Thus, changes in the squeezing capabilities of the two cell types investigated in the current work seem to be due to altered mechanical properties of their nuclei rather than to shared alterations in their transcriptomes. Previous observations showed that depletion of lamin A/C in lung and breast cancer cells, as well as fibrosarcoma cells, significantly increased the likelihood of transient nuclear envelope rupture events and cell death especially when cells were forced to migrate through very tight and rigid barriers (Denais et al., 2016; Harada et al., 2014). Imaging of HT1080 fibrosarcoma cells invading the collagen-rich mouse dermis in live tumors after orthotopic implantation confirmed that migration-induced nuclear envelope rupture occurs in vivo, particularly during cell division (Vargas et al., 2012) and in individually disseminating cells (Denais et al., 2016). Nuclear envelope rupture is less prevalent, however, in cells moving as multicellular collective strands (Denais et al., 2016). Notably, both the melanoma and breast cancer cells studied by us grew and survived normally when orthotopically implanted in their primary organs. In light of their similar in vivo growth, both lamin A/C deficient B16F10 and E0771 cells likely migrate in the skin and mammary tissues as collective strands and are therefore less prone to nuclear envelope rupture and apoptosis. Our results also argue against higher vulnerability of the lamin A/C deficient nuclei in melanoma and breast cancer cells to biochemical or mechanical challenges and nuclear rupture in their primary tissues, i.e., the skin, mammary fat pad. On the other hand, lamin A/C deficient melanoma and breast cancer cells exhibit poor long term survival in the lungs. Collectively, our studies suggest that reduced expression of A-type lamins in multiple types of cancers affect their carcinogenic potential in target organs of metastasis but not in their tissues of origin. Future studies on these cells and on other cancer models should shed more light on the differential roles of these lamins in cancer survival and spread within primary and target organs.

bioRxiv preprint doi: https://doi.org/10.1101/2020.06.23.167130; this version posted June 24, 2020. The copyright holder for this preprint (which was not certified by peer review) is the author/funder, who has granted bioRxiv a license to display the preprint in perpetuity. It is made available under aCC-BY-NC-ND 4.0 International license.

Author Contributions

F.R. designed and performed most of the in vitro and part of the in vivo experiments, analyzed the data and contributed to the writing of the manuscript. O.R. developed the light sheet microscopy-based imaging approaches and performed the in vivo imaging experiments together with M.K. S.W.F. coordinated the mRNA transcriptional experiments and helped writing the manuscript. S.K.Y. performed leukocytes in vitro experiments. N.L. and L.K. conducted in vitro epigenetic studies. Y.A. provided guidance for the LSFM studies. S.O. helped with the in vivo experiments. Y.O. assisted with the SA-β-Gal staining. J.C.S. and S.F.d.A. performed in vitro experiments on global RNA synthesis. E.F. and D.D.-G. performed bioinformatics analysis and graph preparation for RNA-seq data. G.G. supervised the biochemical analysis of heterochromatin and epigenetic enzymes. R.A. supervised all the experiments and wrote the manuscript.

Acknowledgements

We thank Edgar Gomes (Instituto de Medicina Molecular, Lisbon, Portugal), José Fernando Díaz (Centro de Investigaciones Biológicas, CSIC, Madrid, Spain) and Valery Krizhanovsky (Weizmann Institute) for providing reagents and for helpful discussions. We thank Karl-Heinz Altmann for the synthesis of Zampanolide used in our studies. We also thank Dr. Shelly Schwarzbaum for editorial assistance and Anna Aloshin (from the lab of Irit Sagi, WIS) for testing MMP inhibitory activity of GM6001. The RNA-seq work was performed under the guidance of Drs. Merav Kedmi and Hadas Keren-Shaul from the Sandbox unit of the Life Science Core Facility of Weizmann Institute of Science. R.A. is the Incumbent of the Linda Jacobs Chair in Immune and Stem Cell Research. His research is supported by the Israel Science Foundation (grant no. 791/17), the Minerva Foundation, Germany, GIF (grant number I-1470-412.13/2018), as well as grants from the Moross Integrated Cancer Center, Yeda-Sela Center for Basic Research, Helen and Martin Kimmel Institute for Stem Cell Research, the Meyer Henri Cancer Endowment, and from William and Marika Glied and Carol A. Milett. S.N and S.M. are funded by the Wellcome Trust (grant 098291/Z/12/Z to S.N.). G.G's research is supported by an Israel Cancer Association grant no. 20201181.

bioRxiv preprint doi: https://doi.org/10.1101/2020.06.23.167130; this version posted June 24, 2020. The copyright holder for this preprint (which was not certified by peer review) is the author/funder, who has granted bioRxiv a license to display the preprint in perpetuity. It is made available under aCC-BY-NC-ND 4.0 International license.

Figure titles and legends

Figure 1. In vitro real time single cell analysis of tumor transendothelial migration. Differential contribution of melanoma actin and microtubule turnover to transendothelial migration

(A) Serial images of a representative B16F10 cell, labeled with Hoechst, performing transendothelial migration. Time intervals are depicted in each image. The contours of the tumor cell leading edges and nucleus are outlined in each image in yellow and red respectively. See also Movie S1. Scale bar represents 20 µm. (B) Representative images of distinct tumor cell categories (referred to as migratory phenotypes) taken from time lapse videomicroscopy segments of individual B16 cells: round, spread above (SA), forming sub endothelial pseudopodia (SEP), and completing transendothelial migration (TEM). Scale bar represents 20 µm. (C) Migratory phenotypes of B16F10 melanoma, E0771 breast carcinoma and LL/2 Lewis Lung Carcinoma interacting with bEnd.3 monolayers. Values represent the mean ± SEM of three fields in each experimental group (n= 40 cells). The experiment shown is representative of three. See also Movie S2. (D) Relative expression of β1 and β3 integrins in B16F10 cells quantified by FACS. (E) Migratory phenotypes of B16F10 cells interacting with bEnd.3 monolayers in the absence (Isotype Control) or presence of β1+β3 integrin blocking antibodies. n = 40 cells per experimental condition. The experiment shown is representative of three. (F) Effects of jasplakinolide (JASP) or zampanolide (ZMP) on the migratory phenotypes of B16F10 cells. Tumor cells were pretreated with 1 µM JASP for 30 min or with 50 nM ZMP for 3 hours and washed before the TEM assay. Values represent the mean ± SEM of five fields in each experimental group. n = 50 cells per experimental condition. Results shown are from a representative experiment of three. ***p = 0.0002 (round), **p = 0.0070 (unstable SEP), ***p < 0.0001 (stable SEP), **p = 0.0058 (TEM). (G) Effects of ZMP or JASP pretreatments on B16F10 cells spreading on bEnd.3-deposited basement membrane. n = 50 cells per experimental condition. Values represent the mean ± SEM of five fields in each experimental group. Results shown are from a representative experiment of three. **p = 0.0036. See also movie S4. (H) Effects of ZMP or JASP pretreatments on B16F10 cells chemotaxis towards HGF through 8 µm pore transwell filters coated with fibronectin. Values represent the mean ± SEM of five fields in each experimental group. Results shown are from a representative experiment of three. **p = 0.0020 (ZMP), **p = 0.0010 (JASP). (I) Effects of ZMP or JASP pretreatment on B16F10 cells haptotaxis towards fibronectin. Values represent the mean ± SEM of five fields in each experimental group. Results shown are from a representative experiment of two. **p = 0.0011.

bioRxiv preprint doi: https://doi.org/10.1101/2020.06.23.167130; this version posted June 24, 2020. The copyright holder for this preprint (which was not certified by peer review) is the author/funder, who has granted bioRxiv a license to display the preprint in perpetuity. It is made available under aCC-BY-NC-ND 4.0 International license.

Figure 2. Downregulation of lamin A/C increases melanoma squeezing through small rigid pores

(A) Expression levels of lamin A/C and lamin B1 in B16F10 cells transduced with control or lamin A/C shRNA. Glyceraldehyde-3-phosphate dehydrogenase (GAPDH) was used as loading control. (B) Immunostaining of lamin A/C (green) in B16F10 shControl and shLmna cells. Scale bar, 20 µm. (C) Chemotactic migration of B16F10 shControl and shLmna cells through 8 or 3 µm pores transwell filters in presence (+) or absence (-) of HGF (50 ng/ml) for 4 hours. Values represent the mean ± SEM of five fields in each experimental group. Results shown are from a representative experiment of three. ***p = 0.0002 (D) Haptotactic migration of B16F10 shControl and shLmna cells through 8 or 3 µm pores transwell filters in the presence or absence of fibronectin for 4 hours. Values represent the mean ± SEM of five fields in each experimental group. Results shown are from a representative experiment of three. *p = 0.0107, **p = 0.0024.

Figure 3. Downregulation of lamin A/C does not facilitate melanoma TEM but increases tumor nucleus deformability

(A) Migratory phenotypes of control and lamin A/C deficient B16F10 melanoma (shControl and shLmna, respectively) interacting with unstimulated bEnd.3 cells. Values represent the mean ± SEM of four fields in each experimental group (n = 50). The experiments shown are representative of three. (B) Serial images of representative control and lamin A/C deficient B16F10 melanoma cells, labeled with Hoechst. Time intervals are depicted in each image. The contours of the melanoma cell's leading edge and nucleus are outlined in each image in yellow and red respectively. See also Movie S5. (C) Nuclear circularity variation during the distinct indicated phases (1-3) of transendothelial migration of B16F10 shControl and shLmna cells. Values represent the mean ± SEM of six fields in each experimental group (n = 15). The experiment shown is representative of three. *p = 0.0105 (shControl); ****p < 0.0001, *p = 0.0288 (shLmna). The right panel depicts the mean nuclear circularity values for each group of B16F10 cells. The percent changes in mean circularity values are shown on top of the line plots. *p = 0.0152. (D) Nuclear circularity of B16F10 shControl and shLmna cells spread on a bEnd.3-derived basement membrane. n = 50 cells per group. Values are mean ± SEM. ****p < 0.0001. See also Movie S6.

Figure 4. In vivo melanoma crossing of lung capillaries is not enhanced by lamin A/C downregulation

(A) Schematic representation of the LSFM analysis. (B) Visualization of 3D bronchial structures (green, autofluorescence) together with B16 melanoma cells (red, CMTMR) and alveolar capillaries (cyan, CD31). Scale bars, 100 µm. See also Movie S7 (C)

bioRxiv preprint doi: https://doi.org/10.1101/2020.06.23.167130; this version posted June 24, 2020. The copyright holder for this preprint (which was not certified by peer review) is the author/funder, who has granted bioRxiv a license to display the preprint in perpetuity. It is made available under aCC-BY-NC-ND 4.0 International license.

Representative 3D images of intravascular, extravascular, and protrusive tumor cells across the CD31-labeled lung vasculature together with the percentage of B16F10 shControl and shLmna cells present in a volume of $5x10^9$ μm^3 of the left lung lobe (3 hours after injection) counted using Imaris software. The results shown are representative of 3 experiments. Scale bar, 100 µm. See also Movies S8, S9 and S10. (D) Number of B16F10 shControl and shLmna present in the lungs of recipient mice, 3 or 72 hours after i.v. injection. Data are mean ± SEM. The experiment shown is representative of three.

Figure 5. Lamin A/C downregulation reduces heterochromatin content and alters gene transcription

(A) Immunostaining of H3K9me3 (red) in B16F10 shControl and shLmna cells. Hoechst 33258 (cyan) is shown in the left panel. Scale bar, 25 µm. The experiment shown is representative of three. (B) Equal amounts of proteins from B16F10 shControl or shLmna cells, separated by SDS-PAGE and analyzed for the indicated proteins by Western blot analysis. The bar graph represents the mean levels of H3K9me3, H3K27me3 and SUV39H2 normalized to Histone H3 and of SETDB1 normalized to α-Tubulin ± SEM of at least four independent experiments. *$p < 0.05$. (C) Fluorescence microscopy imaging of 5-ethynyl uridine (EU) incorporation (red) and Hoechst 33342 (blue) in B16F10 shControl and shLmna cells. Cells were grown with 1 mM EU for 1 h. The cells were fixed, permeabilized and treated with Alexa Fluor 594 azide. Nucleoplasmic fluorescence intensity of the EU staining was measured using ImageJ. Data from 3 independent experiments are shown in the boxplot. (D) Differentially downregulated (blue), upregulated (red) and non-differentially expressed genes (grey) are shown (LFC > 1 and adjusted p value < 0.05). The names of the top 20 most significantly expressed genes are indicated in the plot. (E) Gene ontology (GO) enrichment analysis of the top differentially downregulated (blue) and upregulated (red) genes in B16F10 shLmna cells. Biological Process (BP), Molecular Function (MF) and Cellular Component (CC).

bioRxiv preprint doi: https://doi.org/10.1101/2020.06.23.167130; this version posted June 24, 2020. The copyright holder for this preprint (which was not certified by peer review) is the author/funder, who has granted bioRxiv a license to display the preprint in perpetuity. It is made available under aCC-BY-NC-ND 4.0 International license.

Figure 6 Melanoma proliferation, response to DNA damage, and senescence are insensitive to lamin A/C downregulation

(A) In vitro cell growth of B16F10 shControl and shLmna cells left in culture without changing the medium. Values represent the mean ± SEM. The experiment shown is representative of three. (B) In vitro cell growth of B16F10 shControl and shLmna cells cultured with growth medium changed every 24 hours. Values represent the mean ± SEM. The experiment shown is representative of three. (C) 15,000 B16F10 shControl and shLmna cells were implanted subcutaneously in flank of C57BL/6 mice. Tumor growth was assessed every other day for 14 days post implantation. The experiment shown is representative of three. (D) 40,000 B16F10 shControl and shLmna cells were injected in the tail of recipient C57BL/6 mice. After 14 days, animals were euthanized and lungs harvested. Surface metastatic foci were macroscopically counted, results are mean ± SEM, n = 5 for each experimental group. *p = 0.0374. A representative lung image from each group is presented. The experiment shown is representative of three. (E) Growth arrest induced by etoposide at different concentrations on B16F10 shControl and shLmna cells after treatment for 72 hours. Values represent the mean ± SEM. The experiment shown is representative of three. (F) Senescence associated β-galactosidase staining of B16F10 shControl and shLmna cells treated with 5 µM etoposide for 72 hours, washed and cultured in regular growth medium for an additional 120 hours. The experiment shown is representative of two. Scale bar, 20 µm. *p = 0.0470.

Figure 7 Effects of lamin A/C downregulation on E0771 migration, growth and metastatic potential

(A) Expression levels of lamin A/C and lamin B1 in E0771 cells transduced with control or lamin A/C shRNA (1 and 2). Glyceraldehyde-3-phosphate dehydrogenase (GAPDH) was used as loading control. (B) Haptotactic migration of E0771 shControl and shLmna cells through 8 or 3 µm pores transwell filters in the presence (+) or absence (-) of fibronectin for 4 hours. Values represent the mean ± SEM of five fields of view in each experimental group. Results shown are from a representative experiment of three. *p = 0.0240 (8 µm) *p = 0.0361 (3 µm). (C) Representative 3D images of intravascular or protrusive tumor cells across the CD31-labeled lung vasculature together with the percentage of E0771 shControl and shLmna cells present in a volume of $5x10^9$ μm^3 of the left lung lobe (3 hours after injection) counted using Imaris software. The results shown are representative of 3 experiments. Scale bar, 100 µm. (D) Differentially downregulated (blue), upregulated (red) and non-differentially expressed genes (grey) are shown (LFC > 1 and adjusted p value < 0.05). The names of the top 20 most significantly expressed genes are indicated in the plot. (E) Gene ontology (GO) enrichment analysis of the top differentially downregulated (blue)

bioRxiv preprint doi: https://doi.org/10.1101/2020.06.23.167130; this version posted June 24, 2020. The copyright holder for this preprint (which was not certified by peer review) is the author/funder, who has granted bioRxiv a license to display the preprint in perpetuity. It is made available under aCC-BY-NC-ND 4.0 International license.

and upregulated (red) genes in E0771 shLmna cells. Biological Process (BP), Molecular Function (MF) and Cellular Component (CC). (F) In vitro cell growth of E0771 shControl and shLmna cells cultured with growth medium changed every 24 hours. Values represent the mean ± SEM. The experiment shown is representative of two. (G) 10,000 E0771 shControl and shLmna cells were implanted in the mammary fat pad of female C57BL/6 mice. Tumor growth was assessed every other day for 14 days post implantation. The experiment shown is representative of three. (H) Growth arrest induced by etoposide at different concentrations on E0771 shControl and shLmna cells after treatment for 72 hours. Values represent the mean ± SEM. The experiment shown is representative of three. (I) Experimental lung metastasis of E0771 breast cancer cells. 20,000 E0771 shControl and shLmna cells were intravenously injected in recipient C57BL/6 mice. After 14 days, animals were euthanized and lungs harvested. The number of micrometastases present in the left lung lobe of each lung was determined. The experiment shown is representative of two. **p = 0.0030. (J) 10,000 E0771 shControl and shLmna cells were intravenously injected in recipient C57BL/6 mice. After 30 days, animals were euthanized and lungs harvested. The number of micrometastases present in the left lung lobe of each lung was determined. The experiment shown is representative of two. *p = 0.0246.

bioRxiv preprint doi: https://doi.org/10.1101/2020.06.23.167130; this version posted June 24, 2020. The copyright holder for this preprint (which was not certified by peer review) is the author/funder, who has granted bioRxiv a license to display the preprint in perpetuity. It is made available under aCC-BY-NC-ND 4.0 International license.

STAR Methods

RESOURCE AVAILABILITY

Lead Contact

Further information and requests for resources and reagents should be directed to and will be fulfilled by the Lead Contact, Ronen Alon (ronen.alon@weizmann.ac.il).

Materials Availability

This study did not generate new unique reagents.

Data and Code Availability

The RNA sequencing data generated during this study are available at GEO, accession code GEO: GSE151176.

EXPERIMENTAL MODEL AND SUBJECT DETAILS

Cells

Murine melanoma (B16F10) and Lewis Lung Carcinoma (LL/2) cells were grown in DMEM supplemented with 10% FBS. Murine breast adenocarcinoma cells (E0771) were grown in DMEM supplemented with 10% FBS, 1 mM sodium pyruvate and 10 mM HEPES. Human embryonic kidney (HEK293T) and murine brain endothelial (bEnd.3) cells were cultured in DMEM medium supplemented with 10% FBS and 2 mM L-glutamine. HDBECs (Human Dermal Blood Endothelial Cells) were grown in endothelial cell growth medium (PromoCell) according to the supplier's instructions and were used at passages 2-3. All the media were supplemented with 1% Penicillin-Streptomycin-Amphotericin B solution. All cell cultures were kept at 37°C in humidified incubator in the presence of 5% CO_2. Human T cells were isolated from citrate-anti-coagulated whole blood of healthy donors by dextran sedimentation and density separation over Ficoll-Paque™ as described (Grabovsky et al., 2000). For generation of T effectors, isolated lymphocytes were seeded on plates coated with anti-CD3 and anti-CD28 mAbs for 48 h in T cell medium (RPMI-1640 supplemented with 10% FBS, 1 mM sodium pyruvate, 2 mM L-glutamine and 50 µM β-mercaptoethanol), and then cultured for 9-12 days in the presence of IL-2 as previously described (Shulman and Alon, 2009). A day before the experiment, effector lymphocytes were washed and incubated overnight in fresh IL-2-containing T cell medium. All in vitro experiments with human leukocytes were approved by the Institutional Review Board of the Weizmann Institute of Science.

Mice

Wild-type mice (WT) on C57BL/6 background were maintained in a pathogen-free facility and all animal procedures were approved by the Animal Care and Use Committee of the Weizmann Institute of Science. Male and female 7- to 8-week-old mice were used in all experiments.

METHOD DETAILS

Imaging and Analysis of Tumor Cell Migration

Murine endothelial bEnd.3 cells ($8x10^4$) were seeded in a µ-Slide VI0.4 ibiTreat (ibidi), pre-coated with gelatin (1% in DDW) for 30 min at 37°C. A day later, B16F10 or E0771 cells were labeled with 20 µM Hoechst 33342 for 5 min at 37°C and resuspended in binding medium (Hank's balanced-salt solution 1X containing 2 mg/ml BSA and 10 mM HEPES, pH 7.4, supplemented with 1 mM $CaCl_2$ and 1 mM $MgCl_2$) and introduced in the ibidi chamber over a confluent bEnd.3 monolayer. Images were acquired at a rate of one frame every 4-5 minutes for 4 hours using an IX83 Inverted Microscope (Olympus) equipped with UPlanFLN 20x/0.50 Ph1 ∞/0.17/FN 26.5 objective (Olympus), 49000-ET-DAPI filter set (Chroma). ORCA-Flash4.0LT camera, model: C11440-42U (Hamamatsu). Temperature was maintained at 37ºC throughout the assay. For analysis of migratory phenotypes, tumor cells in different fields of view (10-15 cells per field) were individually tracked and categorized using cellSense software 1.16 (Olympus). Fiji software was used to determine nuclear circularity of transmigrating tumor cells at different frames of the time-lapse movies. This software was also used to incorporate time codes, labels and scale bars into video segments.

bioRxiv preprint doi: https://doi.org/10.1101/2020.06.23.167130; this version posted June 24, 2020. The copyright holder for this preprint (which was not certified by peer review) is the author/funder, who has granted bioRxiv a license to display the preprint in perpetuity. It is made available under aCC-BY-NC-ND 4.0 International license.

Tumor Cells Transwell Migration Assay

Fibronectin (1.5 µg/ml in PBS) was coated for 30 min at 37°C onto both sides (for tumor chemotaxis assays) or only on the bottom side (for tumor haptotaxis assays) of 8 or 3 µm hanging cell culture inserts (Millipore, MCEP24H48 and MCSP24H48). After washing the filters with PBS, B16F10 or E0771 cells ($4x10^4$) resuspended in DMEM containing 0.1% BSA were introduced into the top chamber. DMEM with 0.1% BSA was inserted in the lower chamber in the presence or absence of the chemoattractant. After 4 or 24 hours at 37°C with CO_2, the cells were fixed with paraformaldehyde (4% in PBS) for 15 min and stained with crystal violet (3% in DDW) for additional 15 min, both at RT. Cells on the upper side of the filter were scraped using a cotton swab whereas cells located on the bottom side were imaged using a SZX16 stereo microscope (Olympus) equipped with SDF PLAPO 1XPF objective (Olympus) set at 10X magnification. DP73 camera (Olympus).

Imaging of Tumor Cell Microtubule Dynamics

B16F10 cells ($1.5x10^5$) were transiently transfected with mCherry-tubulin encoding plasmid using Lipofectamine® 2000, according to the manufacturer's instructions. 24 hours post transfection, the cells were treated with 50 nM zampanolide or DMSO (1:1000 dilution) for 3 hours. Cells were washed twice with warm PBS, removed from the culture plate by trypsinization, labeled with 20 µM Hoechst 33342, resuspended in binding medium (composition described above), and introduced into a µ-Slide VI0.4 ibiTreat (ibidi) over a bEnd.3-deposited basement membrane extracellular matrix (isolated by removal of cultured bEnd.3 cells with 10 mM EDTA 30 min before). Tumor cell images were acquired at a rate of one frame every 4-5 minutes for 1 hour using an IX83 Inverted Microscope (Olympus) equipped with PLAPON 60xOPh/1.4 objective (Olympus), 49008ET - mCherry and 49000 ET - DAPI and filter set (Chroma). ORCA-Flash4.0LT camera, model: C11440-42U (Hamamatsu). Temperature was kept at 37ºC throughout the duration of the assay. Background was subtracted for both the fluorescent channels and 2D-deconvolution was performed in the mCherry channel using cellSense software 1.16 (Olympus). FiJi (SciJava) software was used for title and time code labeling.

Generation of Stable shRNA-Expressing Clones

Lentiviruses were produced by co-transfecting HEK293T cells with the shControl or shLmna vectors and three helper plasmids (Gag-Pol, Rev and VSV-G,) using Lipofectamine® 2000. The virus-containing medium was harvested 48 or 72 hours after transfection and subsequently precleaned by a brief centrifugation at 600 x g and a 0.45 µm filtration. Viruses were collected and concentrated with a precipitation solution (40% PEG8000 and 2.5N NaCl) as described (Guo et al., 2012) and stored at -20°C overnight. A day later, the medium was thawed and centrifuged at 2,400 x g for 30 min at RT. The viral pseudoparticles were resuspended in 200 µl culture medium and mixed with $2.5x10^4$ of tumor cells for 12 hr. 36 hours after viral infection, puromycin was added to the culture medium at a concentration of 2.5 µg/ml (B16F10) or 3 µg/ml (E0771) and tumor cells were selected and expanded, replacing growth medium every 48 hours. The mean knockdown levels were subsequently assessed by Western blotting.

Transient siRNA transfection

B16F10 cells (10^5) were transfected with siRNA (20□nM) using Lipofectamine™ RNAiMAX (Thermo Fisher Scientific) following the manufacturer's instructions. 72 hours after transfection tumor cells were either lysed to quantify the mean knockdown protein levels or utilized in experimental assays. Lamin A/C siRNA (siLmna) sequence used in this study was described in (Roman et al., 2017).

Western Blotting

Cells were grown as described above, washed twice with ice-cold PBS, scraped into lysis buffer (25 mM Tris pH 7.5, 1 mM EDTA, 0.5 mM EGTA, 150 mM NaCl, 1% NP-40, 0.2% SDS, 2 mM Na_3VO_4, 1 mM NaF, 10 mM Nappi, 80 mM b-glycerol phosphate and a protease inhibitor tablet), and kept on ice for 30 min with occasional vortexing. Thereafter, lysates were centrifuged at 14,000 x g for 15 min at 4°C. The supernatant was collected and protein concentration was determined by BCA protein assay (Thermo Fisher Scientific). The protein suspension was separated by gel electrophoresis followed by transfer to nitrocellulose membranes, and blocking with non-fat milk (5% in PBS-T) for 1 hour at RT. Immunoblotting was performed overnight at 4°C according to the manufacturers' guidelines. Antibody binding to membrane blots was detected using horseradish peroxidase conjugated secondary antibodies for 1 hour at RT, followed by development with a chemiluminescence substrate (Thermo Fisher Scientific). Chemiluminescence was detected using the ChemiDoc MP (Bio-Rad Laboratories) imaging system.

bioRxiv preprint doi: https://doi.org/10.1101/2020.06.23.167130; this version posted June 24, 2020. The copyright holder for this preprint (which was not certified by peer review) is the author/funder, who has granted bioRxiv a license to display the preprint in perpetuity. It is made available under aCC-BY-NC-ND 4.0 International license.

Immunofluorescence Staining

B16F10 or E0771 cells ($1.5x10^4$) were seeded into a µ-Slide VI0.4 ibiTreat (ibidi) pre-coated with fibronectin (10 µg/ml in PBS) for 30 min at 37°C. The next day cells were rinsed with ice-cold PBS and fixed with paraformaldehyde (4% in PBS) for 15 min at RT followed by permeabilization with Triton X-100 (0.25% in PBS) for 15 min at RT and blocking with goat serum (10% in PBS) for 20 min at 37°C. The cells were then incubated with anti-lamin A/C antibody (1:100) for 1 hour at RT, washed with ice-cold PBS three times and incubated with an Alexa Fluor 488 conjugated secondary antibody (1:200) for 1 hour at RT. Cells were imaged using an IX83 Inverted Microscope (described above) equipped with an UPlanFLN 40X 0.75 Ph2 ∞/0.17/FN 26.5 objective (Olympus), 49002-ET-EGFP (FITC/Cy2) filter set (Chroma). Alternatively, cells were fixed with paraformaldehyde (3% in PBS) at RT for 5 min followed by fixation in methanol at -20°C for another 5 min. H3K9me3 was detected with rabbit monoclonal anti H3K9me3 and DNA was stained with Hoechst 33258. Immunostaining images were collected using an Olympus IX81 fluorescent microscope equipped with a coolSNAP HQ2 CCD camera (Photometrics).

Imaging of Tumor Cell Nuclear Dynamics

B16F10 or E0771 cells ($2x10^4$) were trypsinized, labeled in suspension with 20 µM Hoechst 33342, resuspended in binding medium (composition described above), and introduced in a µ-Slide VI0.4 ibiTreat (ibidi) over a bEnd.3-deposited basement membrane extracellular matrix. Images were acquired at a rate of one frame every 4-5 minutes for 2 hours using an IX83 Inverted Microscope (described above). Temperature was kept at 37 ºC throughout the duration of the assay. Background was subtracted for the fluorescent channel using cellSense 1.16 (Olympus) software. FiJi (SciJava) software was used for title and time code labeling and determination of the nuclear circularity.

Light Sheet Fluorescent Microscopy of Tumor Cells and Lung Vasculature

B16F10 ($2x10^4$) or E0771 (10^4) cells labeled with CMTMR dye (Thermo Fisher Scientific), 10 µM for 30 min according to the manufacturer's instructions, were injected in the retro-orbital sinus of recipient mice. Euthanasia by administration of sodium pentobarbital (200 mg/Kg) was practiced 3 hours later. Blood capillaries were labeled 15 min before the animal sacrifice by intravenous injection of 6 µg of an Alexa 647-conjugated anti-CD31 mAb. Immediately after the sacrifice, mice were transcardially perfused with PBS and the lungs inflated via the trachea with low gelling agarose (Sigma-Aldrich), subsequently fixed with paraformaldehyde (4% in PBS) for 2 h, dehydrated and cleared using ethyl cinnamate as described in (Klingberg et al., 2017). Cleared intact lung lobes, were imaged using an Ultramicroscope II (LaVision BioTec) operated by the ImspectorPro software (LaVision BioTec). For excitation light sheet was generated by a Superk Super-continuum white light laser (emission 460 nm – 800 nm, 1 mW/nm – 3 (NKT photonics), followed by specific excitation filters per channel. For detection optics microscope was equipped with a single lens configuration - 4X objective - LVBT 4X UM2-BG, with an adjustable refractive index collar set to the RI of 1.56. Images were acquired by an Andor Neo sCMOS camera (2,560 × 2,160, pixel size 6.5 µm x 6.5 µm, Andor). Z stacks were acquired in 3 µm steps. Channel configuration for GFP and EGFP excitation 470\40 emission 525\50, for CMTMR, excitation 560\40 emission 630\75, and for CD31-AF647 excitation 640\30 emission 690\50.

Image Reconstruction and Analysis

Three-dimensional rendering of LSFM was performed via Imaris software (Oxford Instruments). Surfaces of CMTMR-labeled tumor cells were created using volume (comprised between 1000 and 25000 μm^3) and intensity (max of red fluorescent channel) as defining features to unequivocally separate them from background signals. Each cell was individually segmented and its distance was measured with respect to the CD31-labeled blood vessels: intravascular, extravascular or protruding. Supplemental Movies 7-10 were down sampled to accommodate the extremely large original datasets (typically multigigabytes).

Determination of Tumor cell Accumulation in Washed Lungs

B16F10 ($2x10^4$) or E0771 (10^4) cells labeled with 10 µM CMTMR for 30 min according to the manufacturer's instructions, were resuspended in PBS and injected into the retro-orbital sinus of recipient mice. Euthanasia by administration of sodium pentobarbital (200 mg/Kg) was practiced 3 or 72 hours later. Immediately thereafter, mice were transcardially perfused with PBS and the lungs were extracted, minced and incubated in RPMI-1640 containing collagenase type 4 (1.5 mg/ml) and DNase I (20 µg/ml) at 37°C for 45 min. Lung cell suspensions were pushed through a 100 µm cell strainer and centrifuged at 0.2 x g or 5 min at 4°C. RBCs were subsequently lysed with an RBC lysis

bioRxiv preprint doi: https://doi.org/10.1101/2020.06.23.167130; this version posted June 24, 2020. The copyright holder for this preprint (which was not certified by peer review) is the author/funder, who has granted bioRxiv a license to display the preprint in perpetuity. It is made available under aCC-BY-NC-ND 4.0 International license.

buffer (Sigma Aldrich). The cells were resuspended in ice-cold FACS buffer (PBS with 1% BSA, 0.1% sodium azide and 5 mM EDTA), filtered through a 70 µm strainer and analyzed using a CytoFLEX flow cytometer (Beckman Coulter).

5-Ethynyl Uridine (EU) Labeling of Cultured Cells

B16F10 or E0771 (either shControl or shLmna expressing) cells were grown on serum coated glass coverslips. 1 mM EU was added to the culture medium and cells were kept for 1 hour at 37ºC in 5% CO_2. Cells were then washed with PBS and fixed with 3.7% formaldehyde for 15 min at RT. The fixative was removed and cells were washed twice with PBS, followed by permeabilization with 0.5% Triton X-100 for 15 min at RT. Cells were washed twice with PBS and incorporated EU was detected by click chemistry using a fluorescent azide following the manufacturer's guidelines of Click-iT RNA Imaging Kit (Thermo Fisher Scientific). Following the Click-iT reaction (30 min at RT in the dark), cells were rinsed twice with a rinse buffer. Nuclear staining was performed with Hoechst 33342. Cells were imaged using a Zeiss LSM 710 point scanning confocal microscope with stacking acquisition and generation of maximum intensity projection images. Nucleoplasmic fluorescence intensity measurements were performed in Fiji, and statistical significance was assessed through Mann-Whitney U, two-tailed, test.

Bulk MARS-seq protocol and sequencing

RNA was isolated from 10,000 cells from each cell line using Dynabeads® mRNA Direct Kit (Thermo Fisher Scientific). Libraries for RNA-seq were prepared using a modified version of TranSeq, as described (Jaitin et al., 2014). Briefly, RNA was reversed transcribed with MARS-seq barcoded RT primers in a 10 µl volume with the Affinity Script kit (Agilent). Reverse transcription was analyzed by qRT-PCR and samples with a similar CT were pooled (up to eight samples per pool). Each pool was treated with Exonuclease I (NEB) for 30 min at 37°C and cleaned by 1.2× volumes of SPRI beads (Beckman Coulter). Next, the cDNA was converted to double-stranded DNA with a second strand synthesis kit (NEB) in a 20 ml reaction, incubating for 2 h at 16 °C. The product was purified with 1.4× volumes of SPRI beads, eluted in 8 µl and in vitro transcribed (with the beads) at 37 °C overnight for linear amplification using the T7 High Yield RNA polymerase IVT kit (NEB). Following IVT, the DNA template was removed with Turbo DNase I (Ambion) 15 min at 37 °C and the amplified RNA (aRNA) purified with 1.2 volumes of SPRI beads. The aRNA was fragmented by incubating 3 min at 70 °C in Zn^{2+} RNA fragmentation reagents (Ambion) and purified with 2× volumes of SPRI beads. The aRNA was ligated to the MARS-seq ligation adapter with T4 RNA Ligase I (NEB). The reaction was incubated at 22 °C for 2 h. After 1.5× SPRI cleanup, the ligated product was reverse transcribed using Affinity Script RT enzyme (Agilent) and a primer complementary to the ligated adapter. The reaction was incubated for 2 min at 42 °C, 45 min at 50 °C, and 5 min at 85 °C. The cDNA was purified with 1.5× volumes of SPRI beads. The library was completed and amplified through a nested PCR reaction with 0.5 mM of P5_Rd1 and P7_Rd2 primers and PCR ready mix (Kappa Biosystems). The amplified pooled library was purified with 0.7× volumes of SPRI beads to remove primer leftovers. Library concentration was measured with a Qubit fluorometer (Life Technologies) and mean molecule size was determined with a 2200 TapeStation instrument. RNA-seq libraries were sequenced using the Illumina NextSeq® 500 High Output v2 Kit (75 cycles).

Bioinformatics analysis

Samples were demultiplexed using the barcode present in the R2 read. The analysis was performed using the UTAP pipeline (Kohen et al., 2019). In brief, UMI sequences present in the R2 read were inserted in the read name of R1 sequence file using a python script. Cutadapt was used to trim low quality, poly A and adapter sequences (Martin, 2011), (parameters: -a AGATCGGAAGAGCACACGTCTGAACTCCAGTCAC -a "A{10}" –times 2 -u 3 -u -3 -q 20 -m 25). Sequences were mapped to the UCSC mm10 mouse genome using STAR (Dobin et al., 2013) v2.4.2a (parameters: –alignEndsType EndToEnd, –outFilterMismatchNoverLmax 0.05, –twopassMode Basic, –alignSoftClipAtReferenceEnds No). The pipeline quantified the 3' of RefSeq annotated genes (1,000 bases upstream of the 3' end and 100 bases downstream) using HTSeq count (Anders et al., 2015) and a modified Refseq gtf file (downloaded from igenomes UCSC). UMI information was integrated into the BAM files as tags, using a python script. UMI counting was performed after marking duplicates (in-house script) using a modified HTSeq-count. DESeq2 (Love et al., 2014) was used for normalization and detection of differentially expressed genes. Raw p-values were adjusted for multiple testing using the procedure of Benjamini and Hochberg. Genes were considered to be differentially expressed if their mean normalized expression was greater than 5, the absolute value of the log2FoldChange was greater than 1, and the adjusted p-value was less than

bioRxiv preprint doi: https://doi.org/10.1101/2020.06.23.167130; this version posted June 24, 2020. The copyright holder for this preprint (which was not certified by peer review) is the author/funder, who has granted bioRxiv a license to display the preprint in perpetuity. It is made available under aCC-BY-NC-ND 4.0 International license.

0.05. Batch effects were removed from the read counts using the ComBat function from the sva R package (Johnson et al., 2007). The normalized, batch corrected and log2 transformed read counts outputted by ComBat were used to draw plots. K-means clustering of differentially expressed genes was performed using the Partek® Genomics Suite® software, version 6.6 (Partek Inc., St. Louis, MO, USA). Functional analysis of the differentially expressed genes was performed using https://metascape.org/gp/index.html#/main/step1, Metascape (Zhou et al., 2019). Significantly enriched GO terms for up and downregulated genes were extracted from this analysis.

Cell Growth curves

B16F10 or E0771 cells were plated at a low density of 5,000 cells per well in a 6 well plate. Puromycin-containing growth medium was either replaced every 24 h or left unaltered throughout the duration of the assay (72 h). To determine the number, cells were trypsinized and counted by flow cytometer every 24 hours.

Primary Tumor Growth

A suspension of $1.5x10^4$ B16F10 or 10^4 E0771 (either shControl or shLmna expressing) cells in 50 µl of Matrigel® Matrix mixed with PBS (at 1:1 v/v), was inoculated subcutaneously in the flank (B16F10) or in the mammary fat pad (E0771) of recipient mice. Tumor size (volume) was assessed throughout the duration of the experiment, by vernier caliper measurements of length (L) and width (W) and the tumor volume (V) was calculated using the formula: V = (L x W x W)/2. After 14 days, the animals were euthanized by CO_2 inhalation and the tumor was extracted, weighted and fixed in paraformaldehyde (4% in PBS).

Experimental Lung Metastases

B16F10 ($4x10^4$) or E0771 (10^4 or $2x10^4$) either shControl or shLmna expressing cells were suspended in 200 µl PBS + 0.25 mM EDTA and injected into the tail vein of recipient mice. Animals were euthanized by administration of sodium pentobarbital (200 mg/Kg) 14 or 28 days later. Immediately after the sacrifice, mice were transcardially perfused with PBS and the lungs were extracted and visually analyzed for the presence of surface metastatic foci, subsequently stored in 4% PFA for 24 hours and 1% PFA at 4°C for long term storage. Paraffin embedding and H&E staining of 5 µm-thick sections were performed by the histology core unit of the Weizmann Institute of Science. Sections were digitalized using a Pannoramic SCAN II (3DHISTECH) and analyzed using CaseViewer software (3DHISTECH).

Senescence-Associated-β-Galactosidase (SA-β-Gal) Activity

For SA-β-gal activity assay, B16F10 cells (shControl or shLmna) were treated with 5 µM etoposide for 72 hours, washed and left in regular culture medium (containing 2.5 µg/ml of puromycin) for an additional 120 hours. Cells were then fixed with 0.5% glutaraldehyde in PBS for 15 min, washed twice with PBS supplemented with 1 mM $MgCl_2$ (pH 5.5) and stained with PBS containing 1 mM $MgCl_2$ (pH 5.5) and supplemented with 1 mg/ml X-gal, 5 mM $K_3Fe[CN]_6$ and 5 mM $K_4Fe[CN]_6$ for 5 hours at 37°C in the dark, as described (Krizhanovsky et al., 2008). Cells were washed with warm PBS, fixed with 4% paraformaldehyde and imaged using aSZX16 stereo microscope (Olympus) equipped with SDF PLAPO 1XPF objective (Olympus) set at 10X magnification. DP73 camera (Olympus).

Transwell Migration Assay for T cells

Human effector T cells (at a density of $2x10^6$/ml) were treated with 100 nM Zampanolide or carrier control (DMSO) for 6 hours, washed twice and resuspended in binding medium (as described above). $2x10^5$ cells were seeded in the upper chamber of a 6.5 mm transwells with 5.0 µm pore uncoated polycarbonate membrane inserts (Corning, cat# 3421). The bottom chambers were filled with binding medium alone or supplemented with SDF-1α (CXCL12, 100 ng/ml). T cells were allowed to migrate across the filters at 37°C for 30 min. Subsequently, the transwell inserts were removed, the T cells were collected from the bottom chambers and analyzed using a CytoFLEX flow cytometer (Beckman Coulter).

Analysis of Effector T cells Migration Under Shear Flow

HDBECs were plated at confluence on plastic culture dishes spotted with fibronectin (20 µg/ml in PBS) and, a day later, stimulated for 3 hr with IL-1β (2 ng/ml). Endothelial cell-coated plates were assembled in a flow chamber (Shulman and Alon, 2009). Effector T cells pre-treated with 100 nM Zampanolide or carrier control (DMSO) for 6 hours, were washed and perfused over the endothelial

bioRxiv preprint doi: https://doi.org/10.1101/2020.06.23.167130; this version posted June 24, 2020. The copyright holder for this preprint (which was not certified by peer review) is the author/funder, who has granted bioRxiv a license to display the preprint in perpetuity. It is made available under aCC-BY-NC-ND 4.0 International license.

cell monolayer in binding medium (as described above) for 40 s at a shear stress of 1.5 dyn/cm^2 and then subjected to a shear stress of 5 dyn/cm^2 for 10 min. Images were acquired at a rate of four frames per minute using an Olympus IX83 microscope. For analysis of migratory phenotypes, T cells accumulated in at least three fields of view (60 cells per field) were individually tracked and categorized as described (Shulman and Alon, 2009).

QUANTIFICATION AND STATISTICAL ANALYSIS

Data in graphs are represented as means ± SEM. All tests of statistical significance were performed using a two-tailed Student's t-test with GraphPad Prism software, with the exception of analysis of Figure 6C and S10C for which Mann-Whitney U, two-tailed, test was used. Significance was set to $p < 0.05$. Statistical details of experiments can be found in the figure legends. For figures 6D, 6E, 7D and 7E raw p-values were adjusted for multiple testing using the procedure of Benjamini and Hochberg while genes were considered to be differentially expressed if their mean normalized expression was greater than 5, the absolute value of the log2FoldChange was greater than 1, and the adjusted p-value was less than 0.05.

bioRxiv preprint doi: https://doi.org/10.1101/2020.06.23.167130; this version posted June 24, 2020. The copyright holder for this preprint (which was not certified by peer review) is the author/funder, who has granted bioRxiv a license to display the preprint in perpetuity. It is made available under aCC-BY-NC-ND 4.0 International license.

REAGENT or RESOURCE	SOURCE	IDENTIFIER
Antibodies		
Mouse anti-Lamin A/C (4C11)	Cell Signaling Technology	Cat# 4777, RRID:AB_10545756
Rabbit anti-Lamin B1 [EPR8985(B)]	Abcam	Cat# ab133741, RRID:AB_2616597
Mouse anti-GAPDH (6C5)	Millipore	Cat# MAB374, RRID:AB_2107445
Peroxidase-AffiniPure goat anti-mouse IgG (H+L)	Jackson ImmunoResearch Labs	Cat# 115-035-003, RRID:AB_10015289
Peroxidase-AffiniPure goat anti-rabbit IgG (H+L)	Jackson ImmunoResearch Labs	Cat# 111-035-003, RRID:AB_2313567
Alexa Fluor® 488 donkey anti-mouse IgG (H+L)	Thermo Fisher Scientific	Cat# A-21202, RRID:AB_141607
Alexa Fluor® 647 rat anti-CD31 (390)	BioLegend	Cat# 102416, RRID:AB_493410
Arm. hamster anti-CD29 (HMb1-1)	Thermo Fisher Scientific	Cat# 16-0291-85, RRID:AB_657731
Arm. hamster anti-CD61 (2C9.G3)	Thermo Fisher Scientific	Cat# 16-0611-82, RRID:AB_468984
Rabbit anti-trimethyl-Histone H3 (Lys9) (D4W1U)	Cell Signaling Technology	Cat# 13969, RRID:AB_2798355
Rabbit anti-KMT1B/SUV39H2 [EPR18495]	Abcam	Cat# ab190870, RRID:AB_2827544
Rabbit anti-trimethyl Histone H3 (Lys27) (18E9.1)	Millipore	Cat# 05-1951, RRID:AB_11211815
Rabbit anti-Histone H3 (A3S)	Millipore	Cat# 05-928, RRID:AB_492621
Rabbit ESET/SETDB1 (D4M8R)	Cell Signaling Technology	Cat# 93212, RRID:AB_2800200
Mouse anti-alpha Tubulin (DM1A)	Thermo Fisher Scientific	Cat# 62204, RRID:AB_1965960
LEAF™ Purified anti-human CD3 (OKT3)	BioLegend	Cat# 300314, RRID:AB_314050
LEAF™ Purified anti-human CD28 (CD28.2)	BioLegend	Cat# 302914, RRID:AB_314316
Chemicals, Peptides, and Recombinant Proteins		
Zampanolide	Gift from Dr. José Fernando Díaz Pereira, CIB, Spain	N/A
Jasplakinolide	Millipore	Cat# 420107
Etoposide	Sigma-Aldrich	Cat# E1383
GM6001	Sigma-Aldrich	Cat# M5939
Puromycin	Sigma-Aldrich	Cat# P8833
CellTracker™ Orange CMTMR Dye	Thermo Fisher Scientific	Cat# C2927
Hoechst 33342	Thermo Fisher Scientific	Cat# 62249
Hoechst 33258	Sigma-Aldrich	Cat# 861405
X-Gal	Sigma-Aldrich	Cat# 11680293001
Fibronectin	Sigma-Aldrich	Cat# F1141
Gelatin from bovine skin	Sigma-Aldrich	Cat# G9391
Collagenase, Type 4	Worthington Biochemical	Cat# LS004188
DNase I, grade II	Roche	Cat# 10104159001
Recombinant murine HGF	PeproTech	Cat# 315-23
Recombinant murine EGF	PeproTech	Cat# 315-09
Recombinant murine $VEGF_{165}$(VEGF-A)_	PeproTech	Cat# 450-32
Recombinant murine SDF-1α (CXCL12)	PeproTech	Cat# 250-20A
Recombinant human IL-1β	PeproTech	Cat# 200-01B
Recombinant human IL-2	PeproTech	Cat# 200-02
Recombinant human SDF-1α (CXCL12)	PeproTech	Cat# 300-28A
Critical Commercial Assays		
Click-iT™ RNA Alexa Fluor™ 594 Imaging Kit	Thermo Fisher Scientific	**Cat# C10330**
Dynabeads™ mRNA DIRECT™ Purification Kit	Thermo Fisher Scientific	Cat# 61011
SuperSignal™ West Pico PLUS Chemiluminescent Substrate	Thermo Fisher Scientific	Cat# 34577
Deposited Data		
Raw and processed RNA sequencing data	This Paper	GEO: GSE151176
Experimental Models: Cell Lines		
Human: HEK293T	ATCC	ATCC CRL-3216
Human: HDBEC	PromoCell	Cat# C-12211
Murine: bEnd.3	Gift from Britta Engelhardt, Theodor Kocher Institute, University of Bern	ATCC CRL-2299
Murine: B16F10	Gift from Prof. Lea Eisenbach, Weizmann Institute of Science	ATCC CRL-6475
Murine: E0771	Gift from Dr. Ravid Straussman, Weizmann Institute of Science	**CH3BioSystems (cat. # #94A001)**

bioRxiv preprint doi: https://doi.org/10.1101/2020.06.23.167130; this version posted June 24, 2020. The copyright holder for this preprint (which was not certified by peer review) is the author/funder, who has granted bioRxiv a license to display the preprint in perpetuity. It is made available under aCC-BY-NC-ND 4.0 International license.

Murine: LL/2 (LLC1)	Gift from Dr. Ravid Straussman, Weizmann Institute of Science	ATCC CRL-1642
Experimental Models: Organisms/Strains		
Mouse: C57BL/6	The Jackson Laboratory	N/A
Oligonucleotides		
Control siRNA (siControl)	Bioneer	Sequences: (sense) UUCUCCGAACGUGUCACGUtt; (anti-sense) ACGUGACACGUUCGGAGAAtt
Lamin A/C siRNA (siLmna)	Bioneer	Sequences: (sense) GGCUUGUGGAGAUCGAUAAtt; (anti-sense) UUAUCGAUCUCCACAAGCCgc
Recombinant DNA		
MISSION® TRC2 pLKO.5-puro Empty Vector (shControl)	Sigma-Aldrich	Cat# SHC201
MISSION® shRNA plasmid DNA Lamin A/C	Sigma-Aldrich	TRC# TRCN0000317672
mCherry-alpha-tubulin plasmid	Addgene	Plasmid# 49149
Softwares and Algorithms		
cellSens (v1.16)	Olympus	https://www.olympus-lifescience.com
Imaris (v9.5.1)	Oxford Instruments	https://imaris.oxinst.com/packages
CaseViewer 2.3	3DHISTECH	https://www.3dhistech.com/caseviewer
Fiji	SciJava	https://fiji.sc
CytExpert	Beckman Coulter	https://www.beckman.co.il/flow-cytometry/instruments/cytoflex/software
Flowjo (v10.6.1)	FlowJo	https://flowjo.com
Image Lab (v6.0.1)	Bio-Rad Laboratories	https://www.bio-rad.com
GraphPad Prism 6	GraphPad Software	https://www.graphpad.com
R	R Development Core Team	https://www.r-project.org
UTAP pipeline	(Kohen et al., 2019)	https://utap.readthedocs.io
Cutadapt	(Martin, 2011)	https://github.com/marcelm/cutadapt
HTSeq count	(Anders et al., 2015)	https://github.com/htseq/htseq
STAR (v2.4.2a)	(Dobin et al., 2013)	https://github.com/alexdobin/STAR
DESeq2	(Love et al., 2014)	https://github.com/mikelove/DESeq2
Genomics Suite (v6.6)	Partek	https://www.partek.com
ComBat (sva package)	(Johnson et al., 2007)	https://github.com/jtleek/sva-devel/blob/master/R/sva-package.R
Metascape	(Zhou et al., 2019)	https://metascape.org/gp/index.html#/main/step1
Other		
Lipofectamine™ 2000 Transfection Reagent	Thermo Fisher Scientific	Cat# 11668
Lipofectamine™ RNAiMAX	Thermo Fisher Scientific	Cat# 3778075
Matrigel® Matrix	Corning	Cat# 356234
Ethyl Cinnamate (ECi)	Acros Organics	Cat# 103-36-6
Agarose, low gelling temperature	Sigma-Aldrich	Cat# 9045
cOmplete™, Mini, EDTA-free Protease Inhibitor Cocktail	Roche	Cat# 4693159001
Poly(ethylene glycol) (PEG8000)	Sigma-Aldrich	Cat# 81268
Triton X-100	Sigma-Aldrich	Cat# X100
Cell Dissociation Solution	Biological Industries	Cat# 03-071-1B
Ficoll-Paque™ Plus	GE Healthcare	Cat# 17-1440-03
Red Blood Cell Lysing Buffer Hybri-Max™	Sigma-Aldrich	Cat# R7757
Endothelial Cell Growth Medium MV	PromoCell	Cat# C-22020

bioRxiv preprint doi: https://doi.org/10.1101/2020.06.23.167130; this version posted June 24, 2020. The copyright holder for this preprint (which was not certified by peer review) is the author/funder, who has granted bioRxiv a license to display the preprint in perpetuity. It is made available under aCC-BY-NC-ND 4.0 International license.

Supplemental movie legends

Movie S1 Related to figure 1A

Transendothelial migration of B16F10 murine melanoma

Time lapse movie of an Hoechst-labeled B16F10 crossing a bEnd.3 endothelial monolayer. The contours of the tumor cell leading edges and nucleus are outlined in each image in yellow and red respectively. Elapsed time is designated as h:mm:ss. Scale bar, 20 µm

Movie S2 Related to figure 1B

Migratory phenotypes of B16F10 cells over a bEnd.3 endothelium

Time lapse movie divided in four quadrants in which different B16F10 cells display a unique phenotype when interacting with a bEnd.3 endothelial monolayer. Represented clockwise there are Round, Spread Above (SA), subendothelial pseudopodium (SEP) and transendothelial migration (TEM) phenotypes. Elapsed time is designated as h:mm:ss. Scale bar, 20 µm

Movie S3

Transendothelial migration of melanoma versus human Effector T cells

Time lapse movie that compares a B16F10 melanoma cell (left) to a human Effector T cell (right) while undergoing transendothelial migration. Both cells were labeled with Hoechst 33342. The contours of the tumor cell/leukocyte leading edges and nucleus are outlined in each image in yellow and red respectively. Elapsed time is designated as h:mm:ss (left) or mm:ss (right). Scale bars, 20 µm (left), 5 µm (right).

Movie S4 Related to Figure 2B

Imaging of tumor cell microtubule dynamics

B16F10 cells, transiently transfected with mCherry-tubulin (red), were pretreated with carrier control (DMSO) or 50 nM zampanolide for 3 hours. Cells were subsequently washed, detached and allowed to interact with a bEnd.3-deposited basement membrane. Nuclei (blue) were labeled with Hoechst 33342. Elapsed time is designated as h:mm:ss. Scale bar, 10 µm.

Movie S5 Related to Figure 4B

Transendothelial migration of B16F10 shControl vs shLmna cells

Time lapse movie depicting a Hoechst labeled B16F10 cell shControl (left) and shLmna (right) crossing a bEnd.3 endothelium. The contours of the tumor cell leading edges and nucleus are outlined in yellow and red respectively. Elapsed time is designated as h:mm:ss. Scale bar, 20 µm.

Movie S6 Related to Figure 4E

Nuclear deformability of B16F10 shControl vs shLmna cells

Time lapse movie depicting the Hoechst-labeled nuclei (green) of B16F10 shControl (left) and shLmna (right) cells interacting with a bEnd.3-deposited basement membrane. Elapsed time is designated as h:mm:ss. Scale bar, 20 µm.

Movie S7 Related to Figure 5B

Light sheet microscopy of tumor cells, bronchial structures and lung vasculature

Three-dimensional animated visualization of a section of murine lung lobe. CMTMR-labeled tumor cells (red) and autofluorescent bronchial structures (green) can be observed from seconds 0 to 21 (movie length). CD31-labeled lung vasculature (cyan) can be observed from seconds 22-40 (movie length).

Movie S8 Related to Figure 5C

Example of an intravascular B16F10 cell

Three-dimensional animated visualization of a CMTMR-labeled B16F10 cell (red) located inside a CD31-labeled lung vasculature (cyan). Scale bar, 100 µm.

Movie S9 Related to Figure 5C

Example of a protruding B16F10 cell

Three-dimensional animated visualization of a CMTMR-labeled B16F10 cell (red) protruding through the CD31-labeled lung vasculature (cyan). Scale bar, 100 µm

bioRxiv preprint doi: https://doi.org/10.1101/2020.06.23.167130; this version posted June 24, 2020. The copyright holder for this preprint (which was not certified by peer review) is the author/funder, who has granted bioRxiv a license to display the preprint in perpetuity. It is made available under aCC-BY-NC-ND 4.0 International license.

Movie S10 Related to Figure 5C

Example of an extravascular B16F10 cell

Three-dimensional animated visualization of a CMTMR-labeled B16F10 cell (red) located outside the CD31-labeled lung vasculature (cyan). Scale bar, 100 μm

Supplemental table

Table S1

DeSeq2 analysis output and gene expression levels in enriched Gene Ontology terms.

bioRxiv preprint doi: https://doi.org/10.1101/2020.06.23.167130; this version posted June 24, 2020. The copyright holder for this preprint (which was not certified by peer review) is the author/funder, who has granted bioRxiv a license to display the preprint in perpetuity. It is made available under aCC-BY-NC-ND 4.0 International license.

References

Anders, S., Pyl, P.T., and Huber, W. (2015). HTSeq-A Python framework to work with high-throughput sequencing data. Bioinformatics *31*, 166–169.

Aureille, J., Belaadi, N., and Guilluy, C. (2017). Mechanotransduction via the nuclear envelope: a distant reflection of the cell surface. Curr. Opin. Cell Biol. *44*, 59–67.

Barzilai, S., Yadav, S.K., Morrell, S., Roncato, F., Klein, E., Stoler-Barak, L., Golani, O., Feigelson, S.W., Zemel, A., Nourshargh, S., et al. (2017). Leukocytes Breach Endothelial Barriers by Insertion of Nuclear Lobes and Disassembly of Endothelial Actin Filaments. Cell Rep. *18*, 685–699.

Becker, J.S., Nicetto, D., and Zaret, K.S. (2016). H3K9me3-Dependent Heterochromatin: Barrier to Cell Fate Changes. Trends Genet. *32*, 29–41.

Bell, E.S., and Lammerding, J. (2016). Causes and consequences of nuclear envelope alterations in tumour progression. Eur. J. Cell Biol. *95*, 449–464.

Bishop, J.R., Schuksz, M., and Esko, J.D. (2007). Heparan sulphate proteoglycans fine-tune mammalian physiology. Nature *446*, 1030–1037.

Borrego-Pinto, J., Jegou, T., Osorio, D.S., Auradé, F., Gorjánácz, M., Koch, B., Mattaj, I.W., and Gomes, E.R. (2012). Samp1 is a component of TAN lines and is required for nuclear movement. J. Cell Sci. *125*, 1099–1105.

Broers, J.L.V. V., and Ramaekers, F.C.S.S. (2014). The role of the nuclear lamina in cancer and apoptosis. In Advances in Experimental Medicine and Biology, (Springer, New York, NY), pp. 27–48.

Broers, J.L., Raymond, Y., Rot, M.K., Kuijpers, H., Wagenaar, S.S., and Ramaekers, F.C. (1993). Nuclear A-type lamins are differentially expressed in human lung cancer subtypes. Am. J. Pathol. *143*, 211–220.

Bronshtein, I., Kepten, E., Kanter, I., Berezin, S., Lindner, M., Redwood, A.B., Mai, S., Gonzalo, S., Foisner, R., Shav-Tal, Y., et al. (2015). Loss of lamin A function increases chromatin dynamics in the nuclear interior. Nat. Commun. *6*, 8044.

Burke, B., and Stewart, C.L. (2013). The nuclear lamins: flexibility in function. Nat. Rev. Mol. Cell Biol. *14*, 13–24.

Cao, X., Moeendarbary, E., Isermann, P., Davidson, P.M., Wang, X., Chen, M.B., Burkart, A.K., Lammerding, J., Kamm, R.D., and Shenoy, V.B. (2016). A Chemomechanical Model for Nuclear Morphology and Stresses during Cell Transendothelial Migration. Biophys. J. *111*, 1541–1552.

Capo-chichi, C.D., Cai, K.Q., Smedberg, J., Ganjei-Azar, P., Godwin, A.K., and Xu, X.X. (2011). Loss of A-type lamin expression compromises nuclear envelope integrity in breast cancer. Chin J Cancer *30*, 415–425.

bioRxiv preprint doi: https://doi.org/10.1101/2020.06.23.167130; this version posted June 24, 2020. The copyright holder for this preprint (which was not certified by peer review) is the author/funder, who has granted bioRxiv a license to display the preprint in perpetuity. It is made available under aCC-BY-NC-ND 4.0 International license.

Chambers, A.F.A.F., Groom, A.C.A.C., and MacDonald, I.C.I.C. (2002). Dissemination and growth of cancer cells in metastatic sites. Nat Rev Cancer *2*, 563–572.

Chambliss, A.B., Khatau, S.B., Erdenberger, N., Robinson, D.K., Hodzic, D., Longmore, G.D., and Wirtz, D. (2013). The LINC-anchored actin cap connects the extracellular milieu to the nucleus for ultrafast mechanotransduction. Sci Rep *3*, 1087.

Chang, W., Folker, E.S., Worman, H.J., and Gundersen, G.G. (2013). Emerin organizes actin flow for nuclear movement and centrosome orientation in migrating fibroblasts. Mol. Biol. Cell *24*, 3869–3880.

Cho, S., Vashisth, M., Abbas, A., Majkut, S., Vogel, K., Xia, Y., Ivanovska, I.L., Irianto, J., Tewari, M., Zhu, K., et al. (2019). Mechanosensing by the Lamina Protects against Nuclear Rupture, DNA Damage, and Cell-Cycle Arrest. Dev. Cell *49*, 920-935.e5.

Curtis, C., Shah, S.P., Chin, S.F., Turashvili, G., Rueda, O.M., Dunning, M.J., Speed, D., Lynch, A.G., Samarajiwa, S., Yuan, Y., et al. (2012). The genomic and transcriptomic architecture of 2,000 breast tumours reveals novel subgroups. Nature *486*, 346–352.

Dai, W., Jiang, Y., Chen, K., Qiu, J., Sun, J., Zhang, W., Zhou, X., Huang, N., Li, Y., and Li, W. (2017). Effect of etoposide-induced alteration of the Mdm2-Rb signaling pathway on cellular senescence in A549 lung adenocarcinoma cells. Oncol. Lett. *14*, 3935–3940.

Davidson, P.M., Denais, C., Bakshi, M.C., and Lammerding, J. (2014). Nuclear deformability constitutes a rate-limiting step during cell migration in 3-D environments. Cell Mol Bioeng *7*, 293–306.

Dechat, T., Adam, S.A., Taimen, P., Shimi, T., and Goldman, R.D. (2010). Nuclear Lamins. Cold Spring Harb. Perspect. Biol. *2*, a000547–a000547.

Denais, C., and Lammerding, J. (2014). Nuclear mechanics in cancer. Adv Exp Med Biol *773*, 435–470.

Denais, C.M., Gilbert, R.M., Isermann, P., McGregor, A.L., Te Lindert, M., Weigelin, B., Davidson, P.M., Friedl, P., Wolf, K., and Lammerding, J. (2016). Nuclear envelope rupture and repair during cancer cell migration. Science (80-.). *352*, 353–358.

Dobin, A., Davis, C.A., Schlesinger, F., Drenkow, J., Zaleski, C., Jha, S., Batut, P., Chaisson, M., and Gingeras, T.R. (2013). STAR: Ultrafast universal RNA-seq aligner. Bioinformatics *29*, 15–21.

Dou, Z., Xu, C., Donahue, G., Shimi, T., Pan, J.-A., Zhu, J., Ivanov, A., Capell, B.C., Drake, A.M., Shah, P.P., et al. (2015). Autophagy mediates degradation of nuclear lamina. Nature *527*, 105–109.

Dyer, L., and Patterson, C. (2010). Development of the Endothelium: An Emphasis on Heterogeneity. Semin. Thromb. Hemost. *36*, 227–235.

Elosegui-Artola, A., Andreu, I., Beedle, A.E.M., Lezamiz, A., Uroz, M., Kosmalska, A.J., Oria, R., Kechagia, J.Z., Rico-Lastres, P., Le Roux, A.-L., et al. (2017). Force Triggers YAP

bioRxiv preprint doi: https://doi.org/10.1101/2020.06.23.167130; this version posted June 24, 2020. The copyright holder for this preprint (which was not certified by peer review) is the author/funder, who has granted bioRxiv a license to display the preprint in perpetuity. It is made available under aCC-BY-NC-ND 4.0 International license.

Nuclear Entry by Regulating Transport across Nuclear Pores. Cell *171*, 1397-1410.e14.

Etienne-Manneville, S., and Lammerding, J. (2017). Connecting the plasma membrane to the nucleus by intermediate filaments. Mol. Biol. Cell *28*, 695–696.

Fernández-Morera, J.L., Calvanese, V., Rodríguez-Rodero, S., Menéndez-Torre, E., and Fraga, M.F. (2010). Epigenetic regulation of the immune system in health and disease. Tissue Antigens *76*, 431–439.

Field, J.J., Pera, B., Calvo, E., Canales, A., Zurwerra, D., Trigili, C., Rodriguez-Salarichs, J., Matesanz, R., Kanakkanthara, A., Wakefield, S.J., et al. (2012). Zampanolide, a potent new microtubule-stabilizing agent, covalently reacts with the taxane luminal site in tubulin alpha,beta-heterodimers and microtubules. Chem Biol *19*, 686–698.

Friedl, P., Wolf, K., and Lammerding, J. (2011). Nuclear mechanics during cell migration. Curr. Opin. Cell Biol. *23*, 55–64.

Fruleux, A., and Hawkins, R.J. (2016). Physical role for the nucleus in cell migration. J Phys Condens Matter *28*, 363002.

Gonzalez-Granado, J.M., Silvestre-Roig, C., Rocha-Perugini, V., Trigueros-Motos, L., Cibrian, D., Morlino, G., Blanco-Berrocal, M., Osorio, F.G., Freije, J.M., Lopez-Otin, C., et al. (2014). Nuclear envelope lamin-A couples actin dynamics with immunological synapse architecture and T cell activation. Sci Signal *7*, ra37.

Gorelik, L., and Flavell, R.A. (2001). Immune-mediated eradication of tumors through the blockade of transforming growth factor-β signaling in T cells. Nat. Med. *7*, 1118–1122.

Grabovsky, V., Feigelson, S., Chen, C., Bleijs, D.A.A., Peled, A., Cinamon, G., Baleux, F., Arenzana-Seisdedos, F., Lapidot, T., van Kooyk, Y., et al. (2000). Subsecond induction of alpha4 integrin clustering by immobilized chemokines stimulates leukocyte tethering and rolling on endothelial vascular cell adhesion molecule 1 under flow conditions. J Exp Med *192*, 495–506.

Graham, D.M., Andersen, T., Sharek, L., Uzer, G., Rothenberg, K., Hoffman, B.D., Rubin, J., Balland, M., Bear, J.E., and Burridge, K. (2018). Enucleated cells reveal differential roles of the nucleus in cell migration, polarity, and mechanotransduction. J. Cell Biol. *217*, 895–914.

Guo, P., El-Gohary, Y., Prasadan, K., Shiota, C., Xiao, X., Wiersch, J., Paredes, J., Tulachan, S., and Gittes, G.K. (2012). Rapid and simplified purification of recombinant adeno-associated virus. J. Virol. Methods *183*, 139–146.

Harada, T., Swift, J., Irianto, J., Shin, J.W., Spinler, K.R., Athirasala, A., Diegmiller, R., Dingal, P.C.D.P., Ivanovska, I.L., and Discher, D.E. (2014). Nuclear lamin stiffness is a barrier to 3D-migration, but softness can limit survival. Proc. IEEE Annu. Northeast Bioeng. Conf. NEBEC *2014-Decem*, 669–682.

Harr, J.C., Luperchio, T.R., Wong, X., Cohen, E., Wheelan, S.J., and Reddy, K.L. (2015). Directed targeting of chromatin to the nuclear lamina is mediated by chromatin state and A-

bioRxiv preprint doi: https://doi.org/10.1101/2020.06.23.167130; this version posted June 24, 2020. The copyright holder for this preprint (which was not certified by peer review) is the author/funder, who has granted bioRxiv a license to display the preprint in perpetuity. It is made available under aCC-BY-NC-ND 4.0 International license.

type lamins. J. Cell Biol. *208*, 33–52.

Heemskerk, N., Schimmel, L., Oort, C., van Rijssel, J., Yin, T., Ma, B., van Unen, J., Pitter, B., Huveneers, S., Goedhart, J., et al. (2016). F-actin-rich contractile endothelial pores prevent vascular leakage during leukocyte diapedesis through local RhoA signalling. Nat. Commun. *7*.

Irianto, J., Xia, Y., Pfeifer, C.R., Athirasala, A., Ji, J., Alvey, C., Tewari, M., Bennett, R.R., Harding, S.M., Liu, A.J., et al. (2017). DNA Damage Follows Repair Factor Depletion and Portends Genome Variation in Cancer Cells after Pore Migration. Curr. Biol. *27*, 210–223.

Jaitin, D.A., Kenigsberg, E., Keren-Shaul, H., Elefant, N., Paul, F., Zaretsky, I., Mildner, A., Cohen, N., Jung, S., Tanay, A., et al. (2014). Massively parallel single-cell RNA-seq for marker-free decomposition of tissues into cell types. Science (80-.). *343*, 776–779.

Johnson, W.E., Li, C., and Rabinovic, A. (2007). Adjusting batch effects in microarray expression data using empirical Bayes methods. Biostatistics *8*, 118–127.

Joyce, J.A., and Pollard, J.W. (2009). Microenvironmental regulation of metastasis. Nat. Rev. Cancer *9*, 239–252.

Kaufmann, S.H., Mabry, M., Jasti, R., and Shaper, J.H. (1991). Differential expression of nuclear envelope lamins A and C in human lung cancer cell lines. Cancer Res. *51*, 581–586.

Khatau, S.B., Hale, C.M., Stewart-Hutchinson, P.J., Patel, M.S., Stewart, C.L., Searson, P.C., Hodzic, D., and Wirtz, D. (2009). A perinuclear actin cap regulates nuclear shape. Proc Natl Acad Sci U S A *106*, 19017–19022.

Khuon, S., Liang, L., Dettman, R.W., Sporn, P.H.S., Wysolmerski, R.B., and Chew, T.-L. (2010). Myosin light chain kinase mediates transcellular intravasation of breast cancer cells through the underlying endothelial cells: a three-dimensional FRET study. J. Cell Sci. *123*, 431–440.

Kim, D.H., and Wirtz, D. (2015). Cytoskeletal tension induces the polarized architecture of the nucleus. Biomaterials *48*, 161–172.

Kirby, T.J., and Lammerding, J. (2018). Emerging views of the nucleus as a cellular mechanosensor. Nat. Cell Biol. *20*, 373–381.

Klingberg, A., Hasenberg, A., Ludwig-Portugall, I., Medyukhina, A., Männ, L., Brenzel, A., Engel, D.R., Figge, M.T., Kurts, C., and Gunzer, M. (2017). Fully Automated Evaluation of Total Glomerular Number and Capillary Tuft Size in Nephritic Kidneys Using Lightsheet Microscopy. J. Am. Soc. Nephrol. *28*, 452–459.

Kohen, R., Barlev, J., Hornung, G., Stelzer, G., Feldmesser, E., Kogan, K., Safran, M., and Leshkowitz, D. (2019). UTAP: User-friendly Transcriptome Analysis Pipeline. BMC Bioinformatics *20*.

Kong, L., Schafer, G., Bu, H., Zhang, Y., Zhang, Y., and Klocker, H. (2012). Lamin A/C protein is overexpressed in tissue-invading prostate cancer and promotes prostate cancer

bioRxiv preprint doi: https://doi.org/10.1101/2020.06.23.167130; this version posted June 24, 2020. The copyright holder for this preprint (which was not certified by peer review) is the author/funder, who has granted bioRxiv a license to display the preprint in perpetuity. It is made available under aCC-BY-NC-ND 4.0 International license.

cell growth, migration and invasion through the PI3K/AKT/PTEN pathway. Carcinogenesis *33*, 751–759.

Krizhanovsky, V., Yon, M., Dickins, R.A., Hearn, S., Simon, J., Miething, C., Yee, H., Zender, L., and Lowe, S.W. (2008). Senescence of activated stellate cells limits liver fibrosis. Cell *134*, 657–667.

Krull, S., Dörries, J., Boysen, B., Reidenbach, S., Magnius, L., Norder, H., Thyberg, J., and Cordes, V.C. (2010). Protein Tpr is required for establishing nuclear pore-associated zones of heterochromatin exclusion. EMBO J. *29*, 1659–1673.

Kubben, N., Voncken, J.W., Demmers, J., Calis, C., van Almen, G., Pinto, Y., and Misteli, T. (2010). Identification of differential protein interactors of lamin a and progerin. Nucleus *1*, 1–13.

Lammerding, J., Fong, L.G., Ji, J.Y., Reue, K., Stewart, C.L., Young, S.G., and Lee, R.T. (2006). Lamins a and C but not lamin B1 regulate nuclear mechanics. J. Biol. Chem. *281*, 25768–25780.

Liu, B., Wang, Z., Zhang, L., Ghosh, S., Zheng, H., and Zhou, Z. (2013). Depleting the methyltransferase Suv39h1 improves DNA repair and extends lifespan in a progeria mouse model. Nat. Commun. *4*, 1–12.

Lombardi, M.L., and Lammerding, J. (2011). Keeping the LINC: the importance of nucleocytoskeletal coupling in intracellular force transmission and cellular function. Biochem. Soc. Trans. *39*, 1729–1734.

Love, M.I.M.I., Huber, W., and Anders, S. (2014). Moderated estimation of fold change and dispersion for RNA-seq data with DESeq2. Genome Biol *15*, 550.

Maizels, Y., Elbaz, A., Hernandez-Vicens, R., Sandrusy, O., Rosenberg, A., and Gerlitz, G. (2017). Increased chromatin plasticity supports enhanced metastatic potential of mouse melanoma cells. Exp. Cell Res. *357*, 282–290.

Martin, M. (2011). Cutadapt removes adapter sequences from high-throughput sequencing reads. EMBnet.Journal *17*, 10.

Maynard, S., Keijzers, G., Akbari, M., Ezra, M. Ben, Hall, A., Morevati, M., Scheibye-Knudsen, M., Gonzalo, S., Bartek, J., and Bohr, V.A. (2019). Lamin A/C promotes DNA base excision repair. Nucleic Acids Res. *47*, 11709–11728.

Miles, F.L., Pruitt, F.L., van Golen, K.L., and Cooper, C.R. (2008). Stepping out of the flow: capillary extravasation in cancer metastasis. Clin. Exp. Metastasis *25*, 305–324.

Ofer, N., Mogilner, A., and Keren, K. (2011). Actin disassembly clock determines shape and speed of lamellipodial fragments. Proc Natl Acad Sci U S A *108*, 20394–20399.

Raab, M., Gentili, M., de Belly, H., Thiam, H.R., Vargas, P., Jimenez, A.J., Lautenschlaeger, F., Voituriez, R., Lennon-Dumenil, A.M., Manel, N., et al. (2016). ESCRT III repairs nuclear envelope ruptures during cell migration to limit DNA damage and cell death. Science (80-.).

bioRxiv preprint doi: https://doi.org/10.1101/2020.06.23.167130; this version posted June 24, 2020. The copyright holder for this preprint (which was not certified by peer review) is the author/funder, who has granted bioRxiv a license to display the preprint in perpetuity. It is made available under aCC-BY-NC-ND 4.0 International license.

352, 359–362.

Reymond, N., Im, J.H., Garg, R., Vega, F.M., Borda d'Agua, B., Riou, P., Cox, S., Valderrama, F., Muschel, R.J., and Ridley, A.J. (2012). Cdc42 promotes transendothelial migration of cancer cells through β1 integrin. J. Cell Biol. *199*, 653–668.

Reymond, N., d'Agua, B.B., and Ridley, A.J. (2013). Crossing the endothelial barrier during metastasis. Nat Rev Cancer *13*, 858–870.

Roman, W., Martins, J.P., Carvalho, F.A., Voituriez, R., Abella, J.V.G., Santos, N.C., Cadot, B., Way, M., and Gomes, E.R. (2017). Myofibril contraction and crosslinking drive nuclear movement to the periphery of skeletal muscle. Nat. Cell Biol. *19*, 1189–1201.

Rowat, A.C., Jaalouk, D.E., Zwerger, M., Ung, W.L., Eydelnant, I.A., Olins, D.E., Olins, A.L., Herrmann, H., Weitz, D.A., and Lammerding, J. (2013). Nuclear envelope composition determines the ability of neutrophil-type cells to passage through micron-scale constrictions. J Biol Chem *288*, 8610–8618.

Scaffidi, P., and Misteli, T. (2006). Lamin A-dependent nuclear defects in human aging. Science (80-.). *312*, 1059–1063.

Shin, J.W., Spinler, K.R., Swift, J., Chasis, J.A., Mohandas, N., and Discher, D.E. (2013). Lamins regulate cell trafficking and lineage maturation of adult human hematopoietic cells. Proc Natl Acad Sci U S A *110*, 18892–18897.

Shulman, Z., and Alon, R. (2009). Chapter 14. Real-time in vitro assays for studying the role of chemokines in lymphocyte transendothelial migration under physiologic flow conditions. Methods Enzym. *461*, 311–332.

Shulman, Z., and Alon, R. (2012). Real-time analysis of integrin-dependent transendothelial migration and integrin-independent interstitial motility of leukocytes. Methods Mol Biol *757*, 31–45.

Solovei, I., Wang, A.S., Thanisch, K., Schmidt, C.S., Krebs, S., Zwerger, M., Cohen, T.V., Devys, D., Foisner, R., Peichl, L., et al. (2013). LBR and Lamin A/C Sequentially Tether Peripheral Heterochromatin and Inversely Regulate Differentiation. Cell *152*, 584–598.

Stephens, P.J., Tarpey, P.S., Davies, H., Van Loo, P., Greenman, C., Wedge, D.C., Nik-Zainal, S., Martin, S., Varela, I., Bignell, G.R., et al. (2012). The landscape of cancer genes and mutational processes in breast cancer. Nature *486*, 400–404.

Sullivan, T., Escalante-Alcalde, D., Bhatt, H., Anver, M., Bhat, N., Nagashima, K., Stewart, C.L., and Burke, B. (1999). Loss of A-type lamin expression compromises nuclear envelope integrity leading to muscular dystrophy. J. Cell Biol. *147*, 913–919.

Swift, J., Ivanovska, I.L., Buxboim, A., Harada, T., Dingal, P.C., Pinter, J., Pajerowski, J.D., Spinler, K.R., Shin, J.W., Tewari, M., et al. (2013). Nuclear lamin-A scales with tissue stiffness and enhances matrix-directed differentiation. Science (80-.). *341*, 1240104.

Towbin, B.D., Meister, P., and Gasser, S.M. (2009). The nuclear envelope--a scaffold for

bioRxiv preprint doi: https://doi.org/10.1101/2020.06.23.167130; this version posted June 24, 2020. The copyright holder for this preprint (which was not certified by peer review) is the author/funder, who has granted bioRxiv a license to display the preprint in perpetuity. It is made available under aCC-BY-NC-ND 4.0 International license.

silencing? Curr. Opin. Genet. Dev. *19*, 180–186.

Valastyan, S., and Weinberg, R.A. (2011). Tumor Metastasis: Molecular Insights and Evolving Paradigms. Cell *147*, 275–292.

Vargas, J.D., Hatch, E.M., Anderson, D.J., and Hetzer, M.W. (2012). Transient nuclear envelope rupturing during interphase in human cancer cells. Nucleus *3*, 88–100.

Venables, R.S., McLean, S., Luny, D., Moteleb, E., Morley, S., Quinlan, R.A., Lane, E.B., and Hutchison, C.J. (2001). Expression of individual lamins in basal cell carcinomas of the skin. Br. J. Cancer *84*, 512–519.

Weinstein, J.N., Collisson, E.A., Mills, G.B., Shaw, K.R.M., Ozenberger, B.A., Ellrott, K., Sander, C., Stuart, J.M., Chang, K., Creighton, C.J., et al. (2013). The cancer genome atlas pan-cancer analysis project. Nat. Genet. *45*, 1113–1120.

Wilson, K.L., and Berk, J.M. (2010). The nuclear envelope at a glance. J. Cell Sci. *123*, 1973–1978.

Wilson, K.L., and Foisner, R. (2010). Lamin-binding Proteins. Cold Spring Harb. Perspect. Biol. *2*, a000554.

Wolf, K., Te Lindert, M., Krause, M., Alexander, S., Te Riet, J., Willis, A.L., Hoffman, R.M., Figdor, C.G., Weiss, S.J., and Friedl, P. (2013). Physical limits of cell migration: control by ECM space and nuclear deformation and tuning by proteolysis and traction force. J Cell Biol *201*, 1069–1084.

Yadav, S.K., Feigelson, S.W., Roncato, F., Antman-Passig, M., Shefi, O., Lammerding, J., and Alon, R. (2018). Frontline Science: Elevated nuclear lamin A is permissive for granulocyte transendothelial migration but not for motility through collagen I barriers. J. Leukoc. Biol. *104*, 239–251.

Yadav, S.K., Stojkov, D., Feigelson, S.W., Roncato, F., Simon, H.-U., Yousefi, S., and Alon, R. (2019). Chemokine triggered microtubule polymerization promotes neutrophil chemotaxis and invasion but not transendothelial migration. J. Leukoc. Biol. *105*, 755–766.

Zhou, Y., Zhou, B., Pache, L., Chang, M., Khodabakhshi, A.H., Tanaseichuk, O., Benner, C., and Chanda, S.K. (2019). Metascape provides a biologist-oriented resource for the analysis of systems-level datasets. Nat. Commun. *10*, 1523.

bioRxiv preprint doi: https://doi.org/10.1101/2020.06.23.167130; this version posted June 24, 2020. The copyright holder for this preprint (which was not certified by peer review) is the author/funder, who has granted bioRxiv a license to display the preprint in perpetuity. It is made available under aCC-BY-NC-ND 4.0 International license.

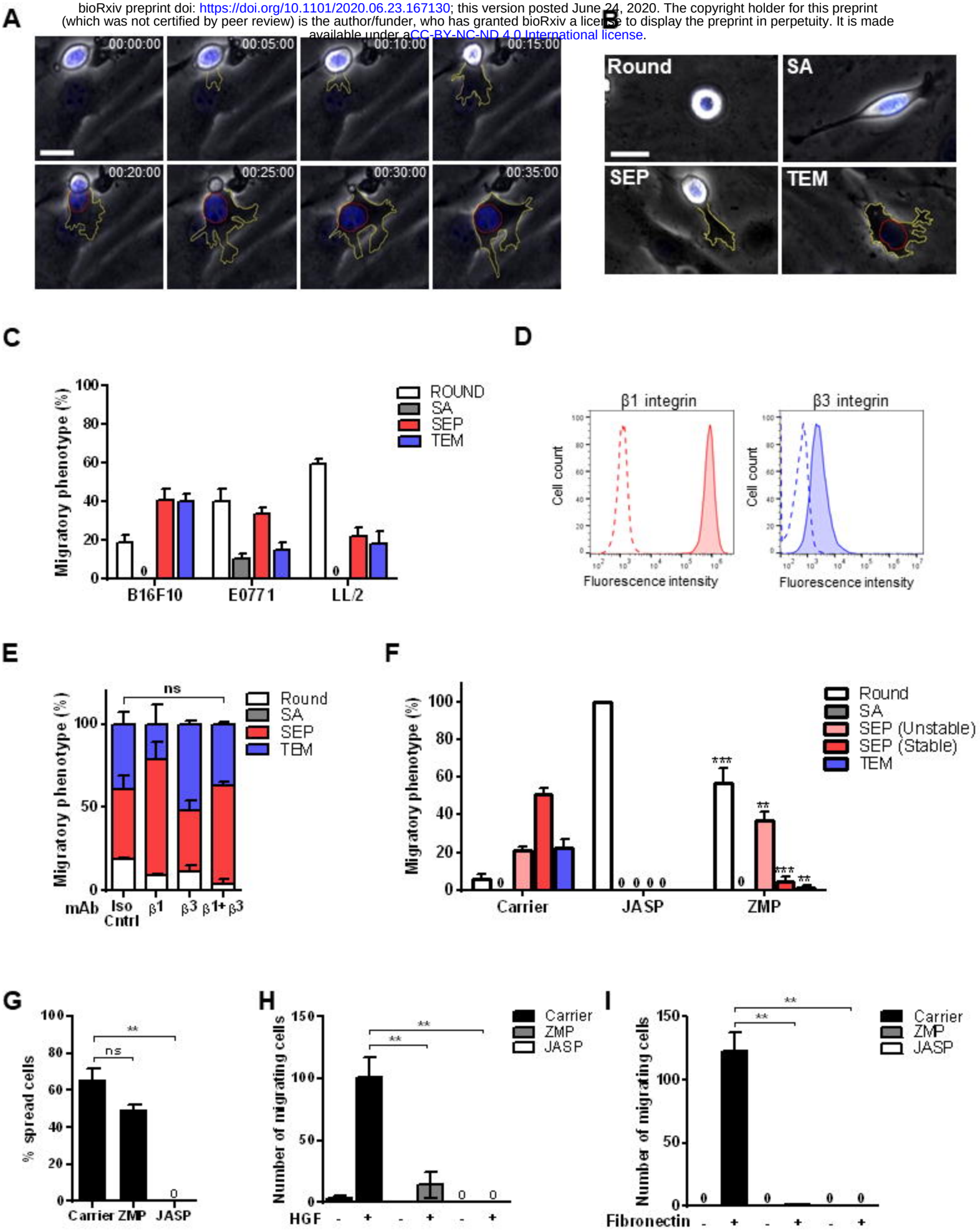

Figure 1

bioRxiv preprint doi: https://doi.org/10.1101/2020.06.23.167130; this version posted June 24, 2020. The copyright holder for this preprint (which was not certified by peer review) is the author/funder, who has granted bioRxiv a license to display the preprint in perpetuity. It is made available under aCC-BY-NC-ND 4.0 International license.

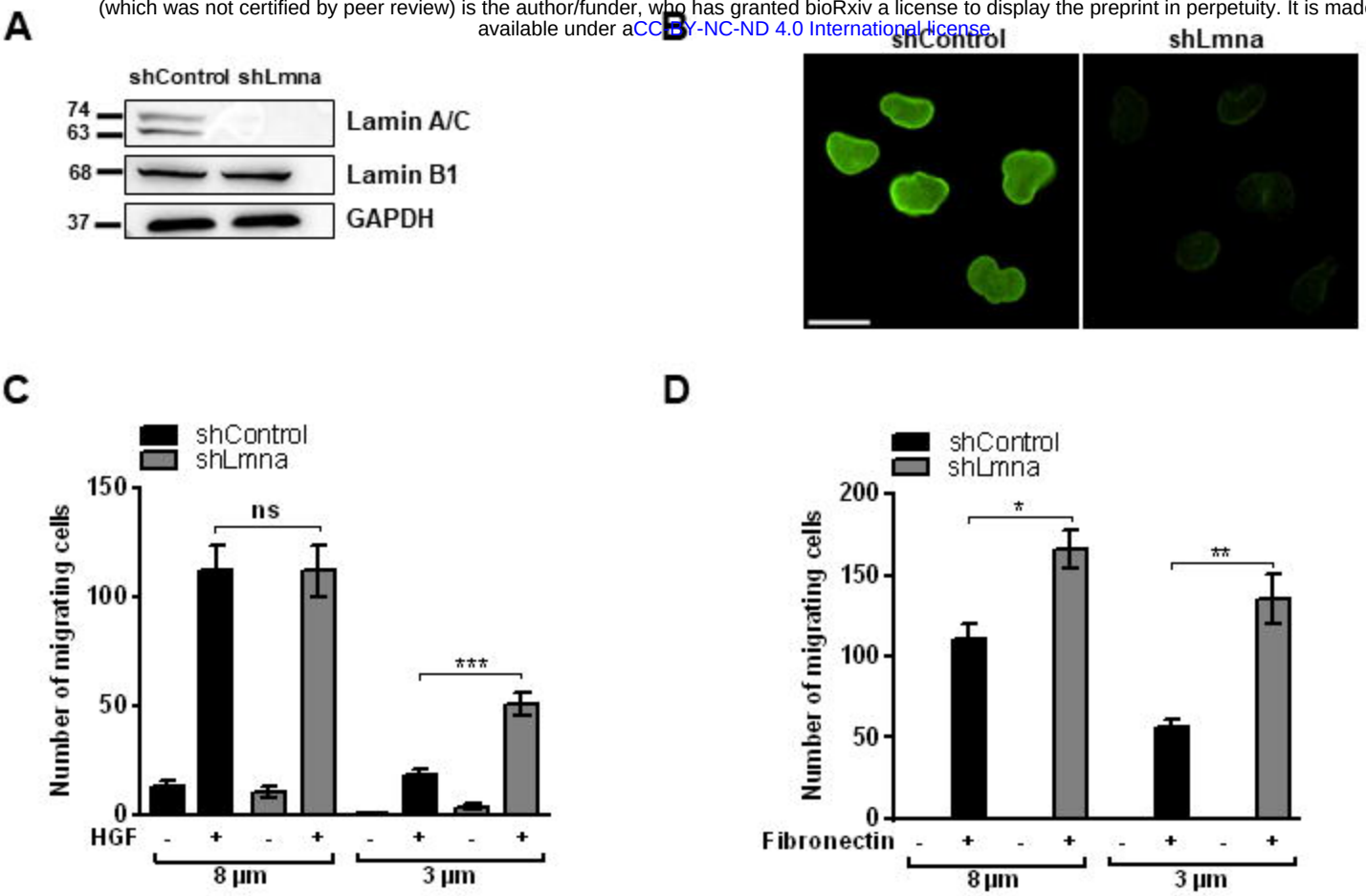

Figure 2

bioRxiv preprint doi: https://doi.org/10.1101/2020.06.23.167130; this version posted June 24, 2020. The copyright holder for this preprint (which was not certified by peer review) is the author/funder, who has granted bioRxiv a license to display the preprint in perpetuity. It is made available under aCC-BY-NC-ND 4.0 International license.

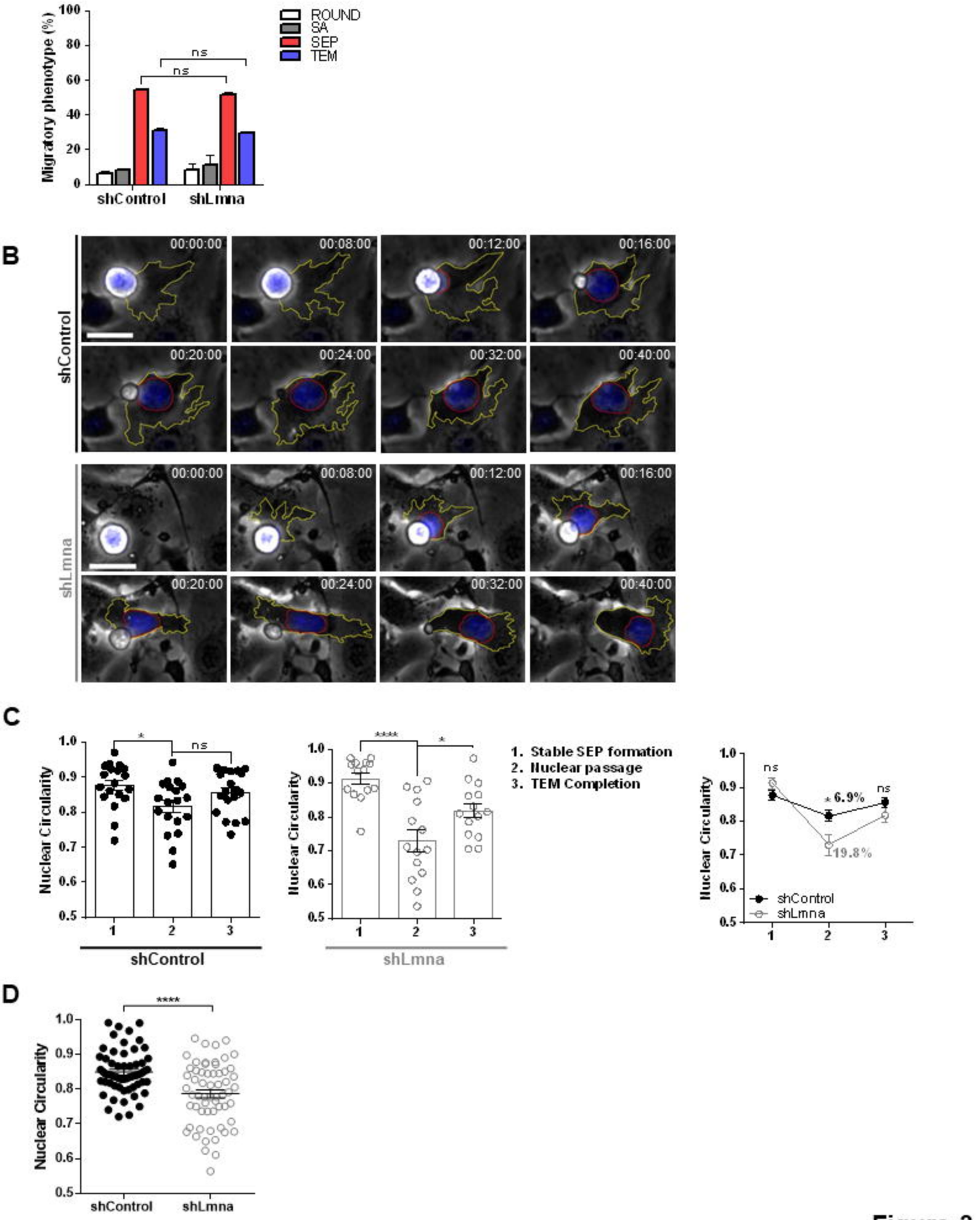

Figure 3

bioRxiv preprint doi: https://doi.org/10.1101/2020.06.23.167130; this version posted June 24, 2020. The copyright holder for this preprint (which was not certified by peer review) is the author/funder, who has granted bioRxiv a license to display the preprint in perpetuity. It is made available under aCC-BY-NC-ND 4.0 International license.

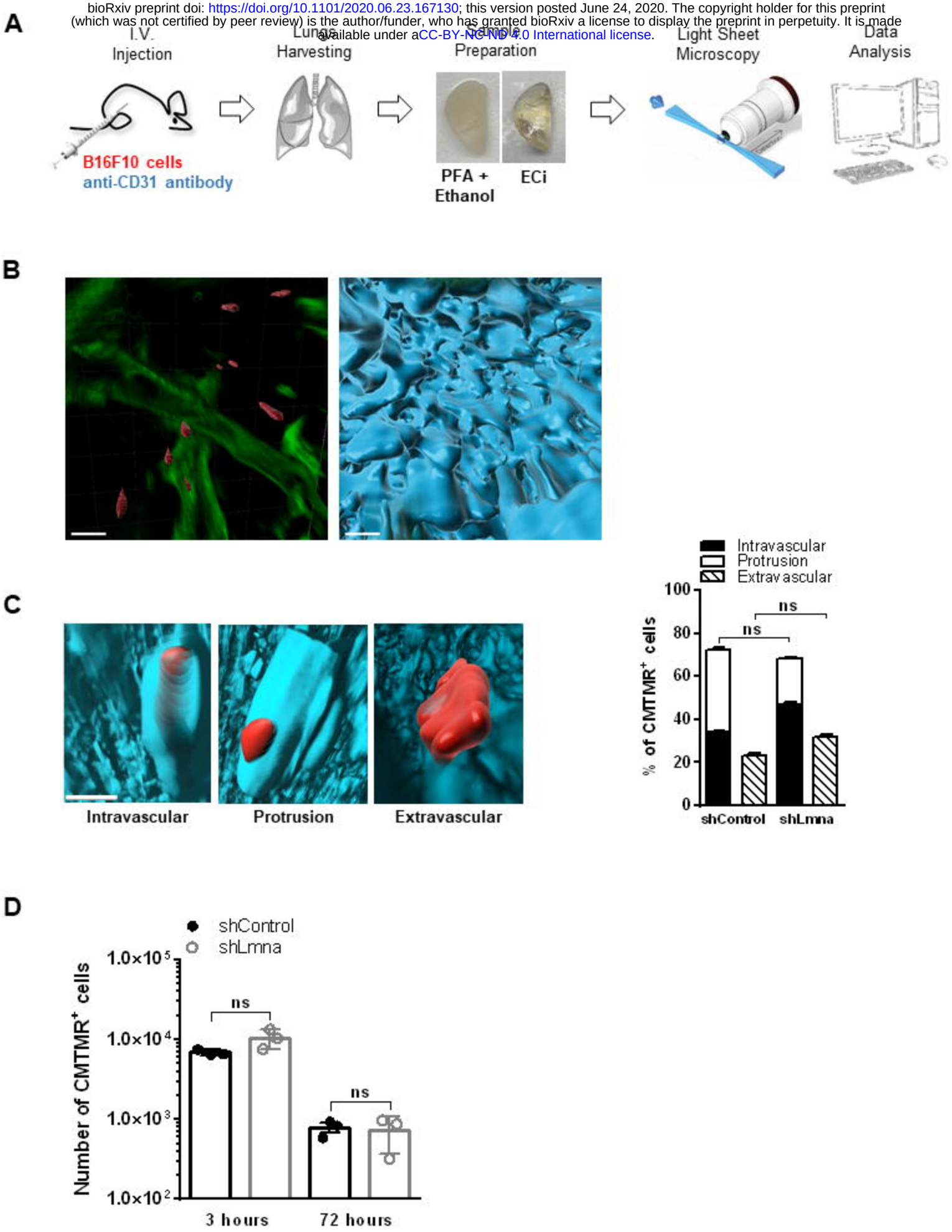

Figure 4

bioRxiv preprint doi: https://doi.org/10.1101/2020.06.23.167130; this version posted June 24, 2020. The copyright holder for this preprint (which was not certified by peer review) is the author/funder, who has granted bioRxiv a license to display the preprint in perpetuity. It is made available under aCC-BY-NC-ND 4.0 International license.

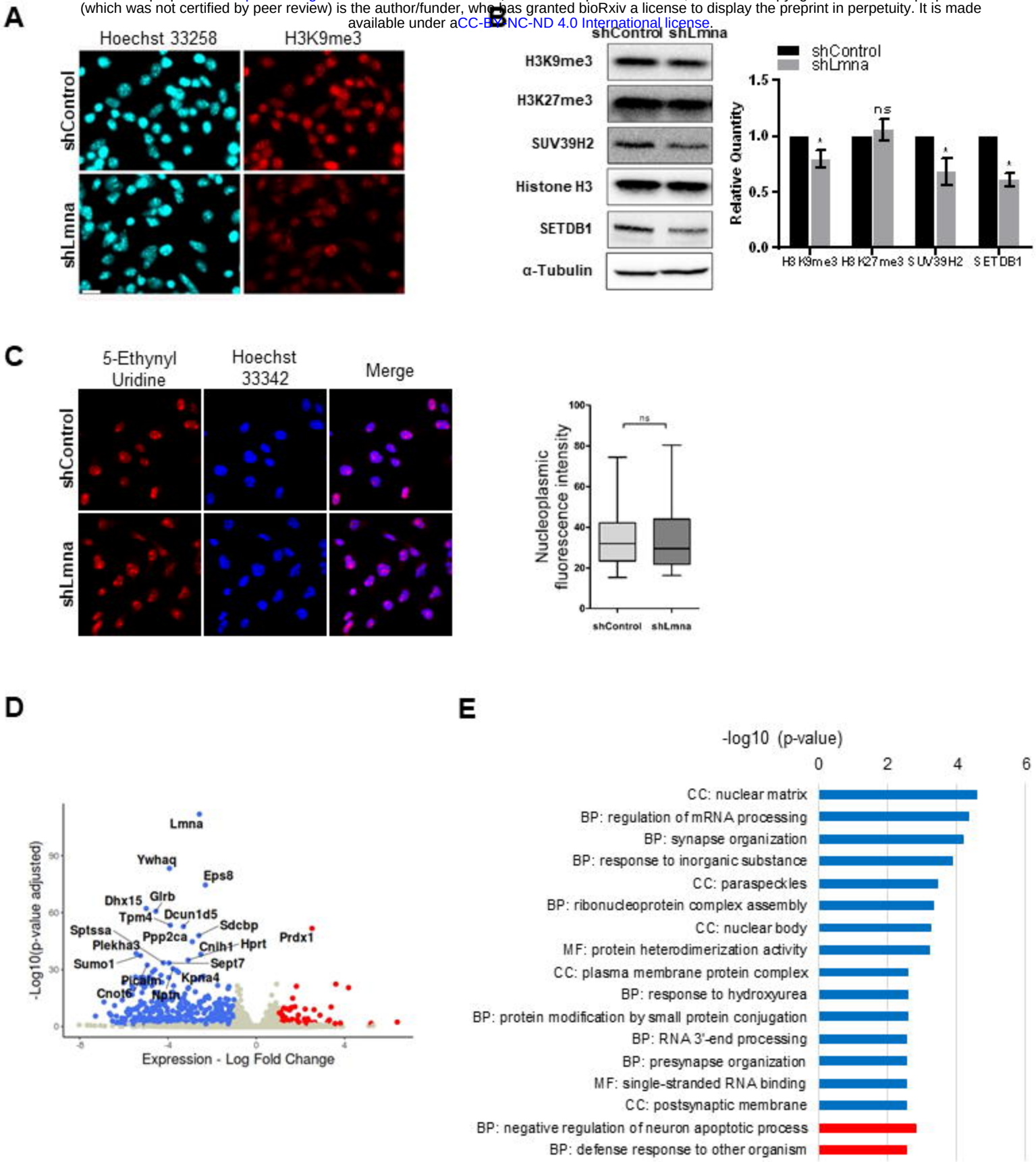

Figure 5

bioRxiv preprint doi: https://doi.org/10.1101/2020.06.23.167130; this version posted June 24, 2020. The copyright holder for this preprint (which was not certified by peer review) is the author/funder, who has granted bioRxiv a license to display the preprint in perpetuity. It is made available under aCC-BY-NC-ND 4.0 International license.

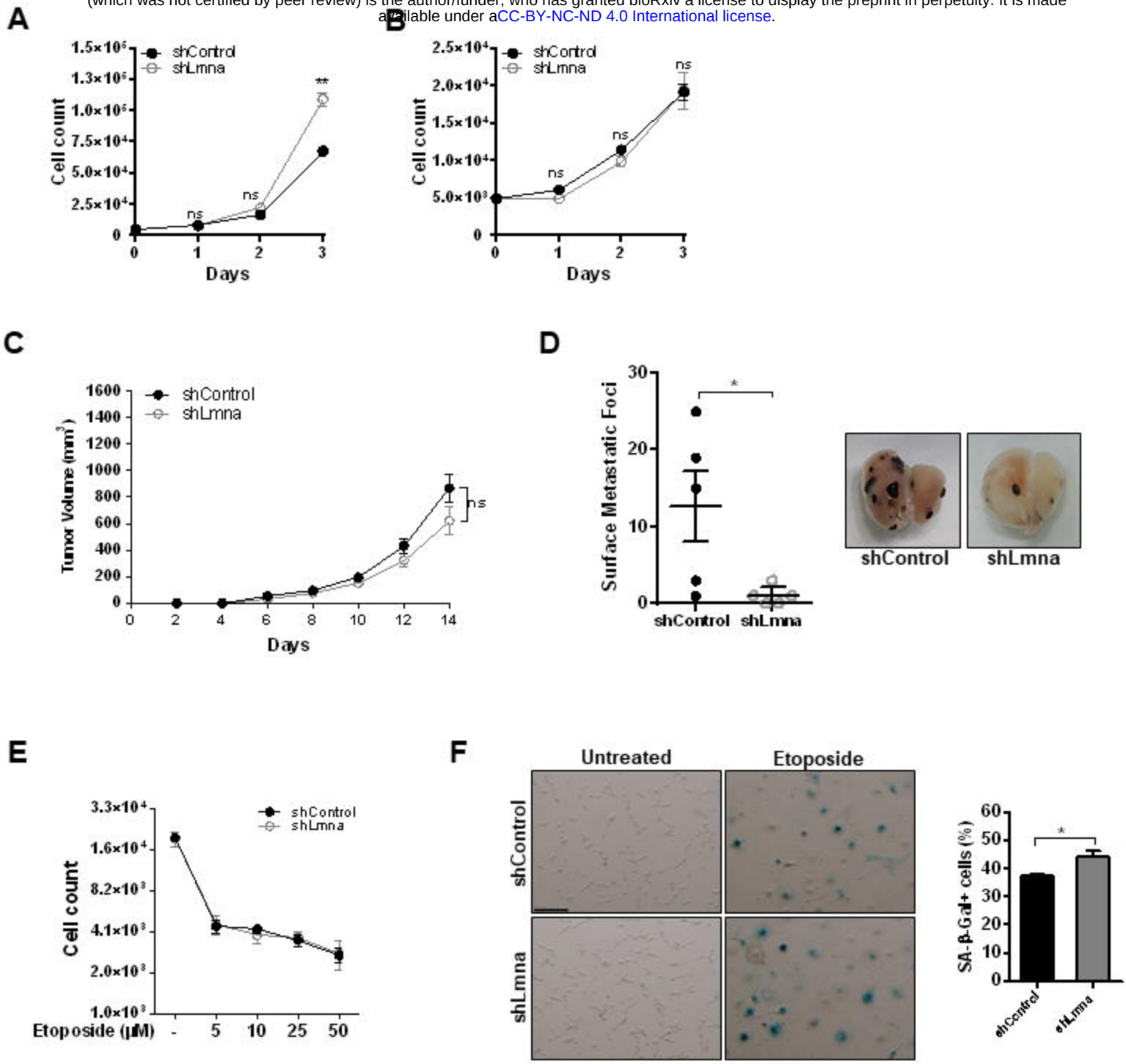

Figure 6

bioRxiv preprint doi: https://doi.org/10.1101/2020.06.23.167130; this version posted June 24, 2020. The copyright holder for this preprint (which was not certified by peer review) is the author/funder, who has granted bioRxiv a license to display the preprint in perpetuity. It is made available under aCC-BY-NC-ND 4.0 International license.

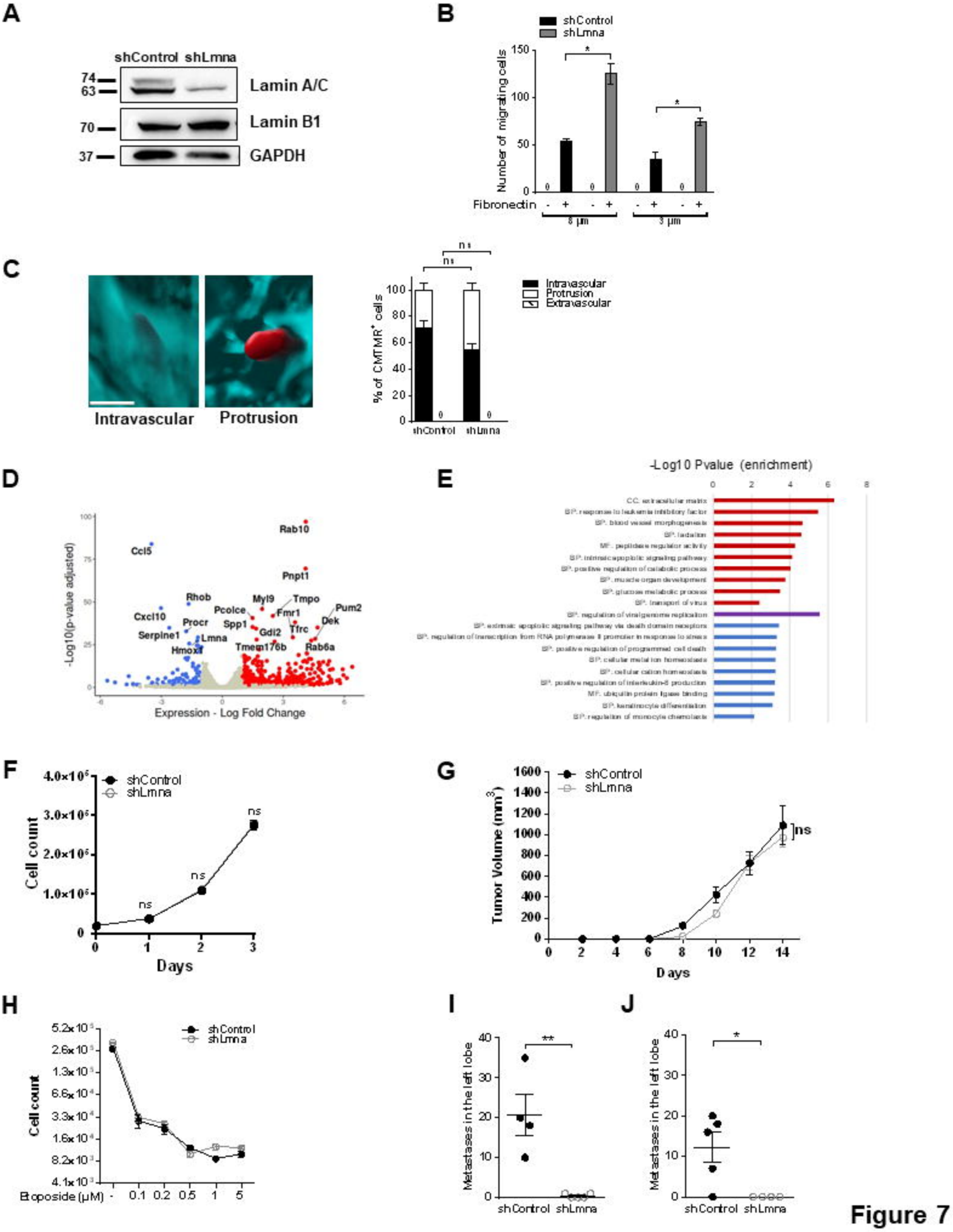

Figure 7

bioRxiv preprint doi: https://doi.org/10.1101/2020.06.23.167130; this version posted June 24, 2020. The copyright holder for this preprint (which was not certified by peer review) is the author/funder, who has granted bioRxiv a license to display the preprint in perpetuity. It is made available under aCC-BY-NC-ND 4.0 International license.

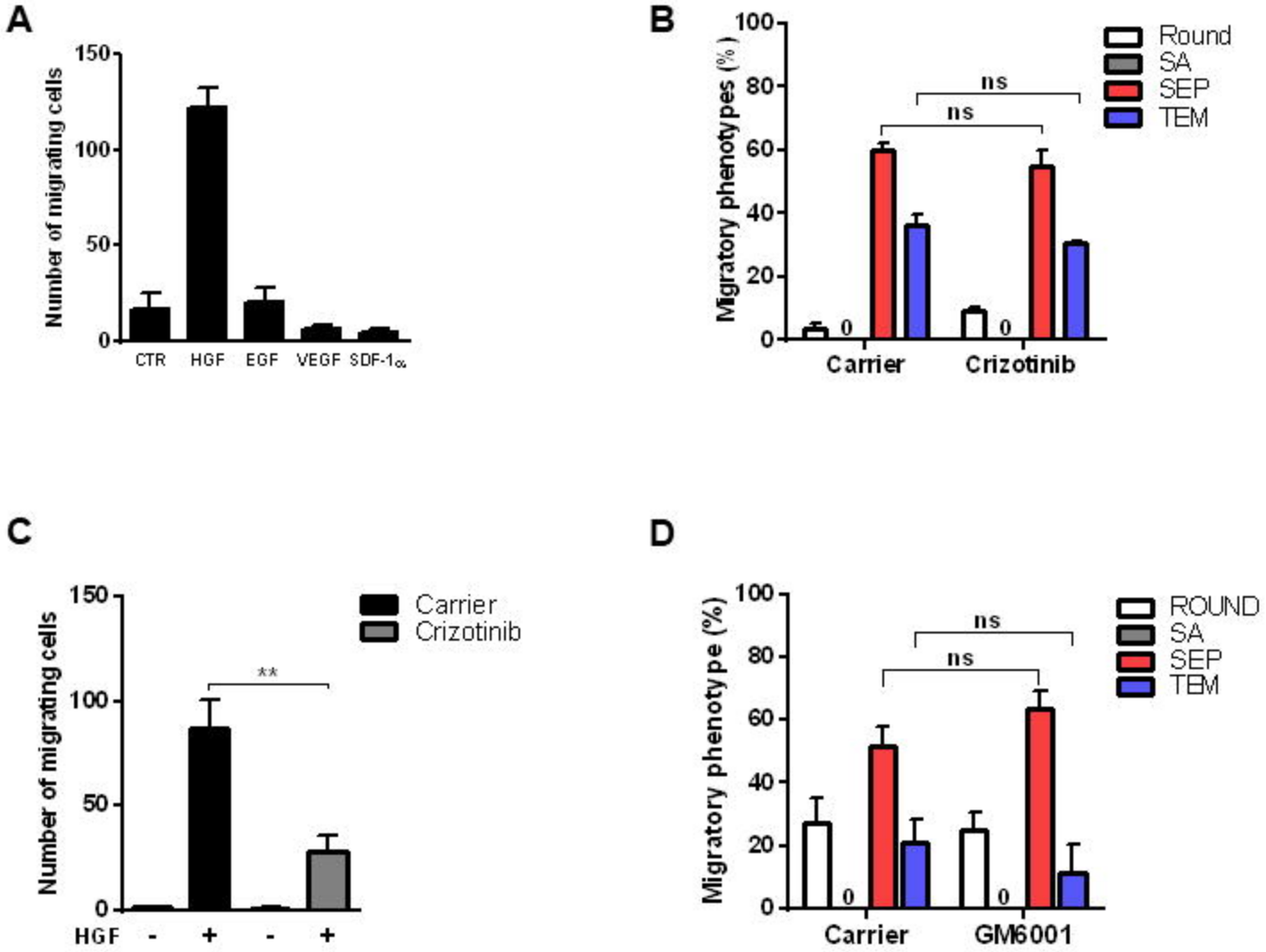

Figure S1. B16F10 TEM is c-Met and MMPs independent.
(A) Number of migrating B16F10 cells through 8 µm pore transwell filters coated on both sides with fibronectin (1.5 µg/ml). The indicated attractants HGF (50 ng/ml), EGF (10 ng/ml), VEGF (25 ng/ml) or SDF-1α (100 ng/ml), were added to the bottom chamber. Results are mean ± SEM of 6 fields of view. A representative experiment of three. (B) Effect of the c-Met inhibitor Crizotinib on B16F10 TEM. (C) Effect of the c-Met inhibitor on B16F10 cell transwell migration through 8 µm pore transwell filters coated on both sides with Fibronectin (1.5 µg/ml) towards HGF (50 ng/ml). Melanoma cells were pretreated with 30 nM Crizotinib for 1 hour and the inhibitor was left in the medium throughout the TEM and chemotaxis assays (4 hours each). Representatives of three experiments. **p = 0.0048. (D) Effect of the pan MMP inhibitor GM6001 on B16F10 TEM. Tumor cells were pretreated with 25 µM GM6001 for 2 hours, and the inhibitor was kept in the medium throughout the the assay. The compound was confirmed to inhibit the activity of purified MMP-9 with an IC50 of 0.75 nM in an in vitro assay using a fluorogenic peptide as substrate. The experiment is representative of three.

bioRxiv preprint doi: https://doi.org/10.1101/2020.06.23.167130; this version posted June 24, 2020. The copyright holder for this preprint (which was not certified by peer review) is the author/funder, who has granted bioRxiv a license to display the preprint in perpetuity. It is made available under aCC-BY-NC-ND 4.0 International license.

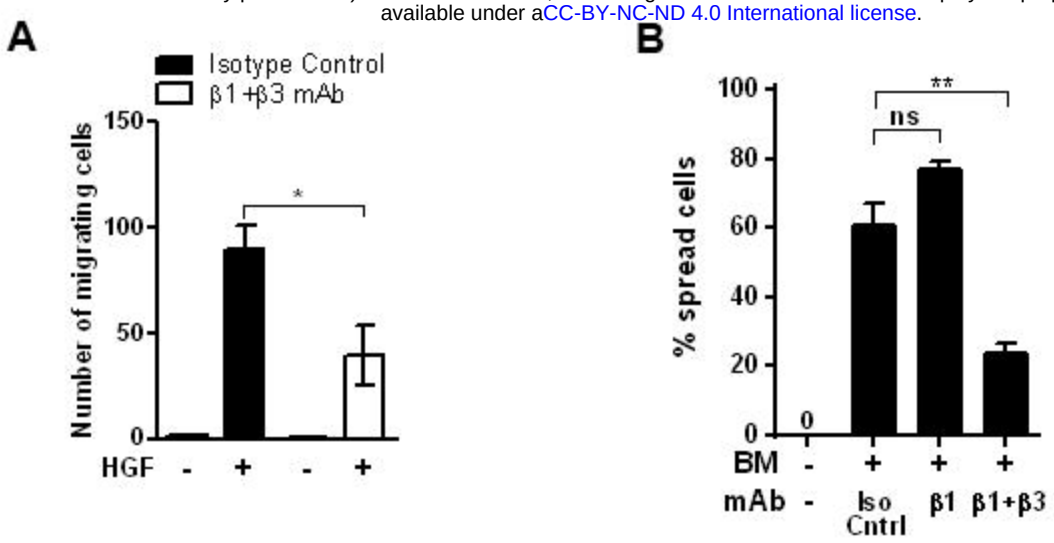

Figure S2. Chemotaxis analysis of B16 melanoma cells in vitro.
(A) Effect of integrin blocking on B16F10 chemotaxis towards HGF (50 ng/ml) through 8 μm pore transwell filters coated with fibronectin. The number of migrating B16 cells recovered in the lower side of the filter after 4 hours was determined in triplicates. *p = 0.0228. (B) Percent of B16F10 cells spread over bEnd.3-deposited basement membrane (BM+) or control gelatin without BM coating (BM-) in the absence (Isotype Control) or presence of the indicated integrin blocking mAbs. n = 50 cells per experimental condition. **p = 0.0021.

bioRxiv preprint doi: https://doi.org/10.1101/2020.06.23.167130; this version posted June 24, 2020. The copyright holder for this preprint (which was not certified by peer review) is the author/funder, who has granted bioRxiv a license to display the preprint in perpetuity. It is made available under aCC-BY-NC-ND 4.0 International license.

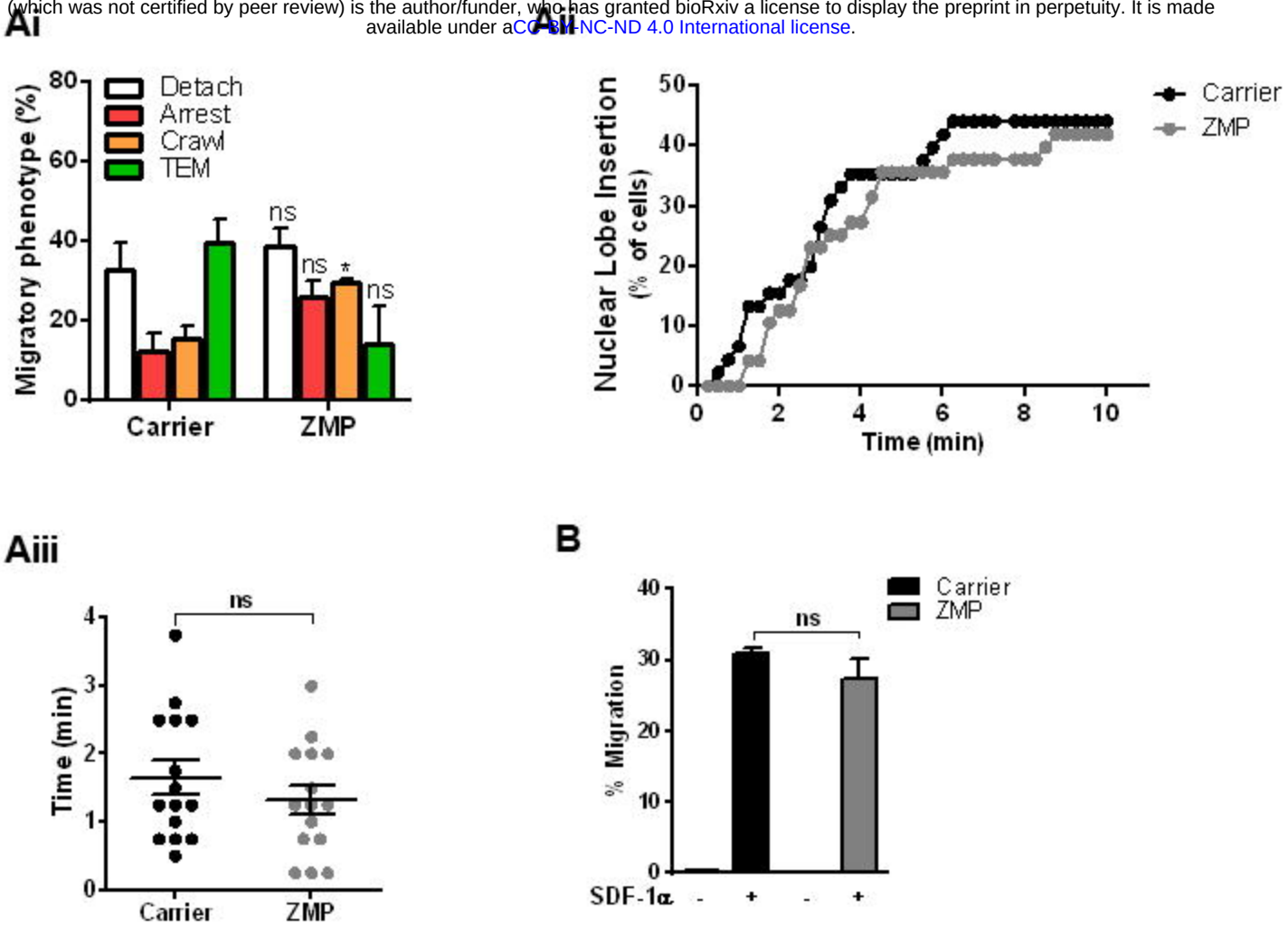

Figure S3. ZMP mildly affects human effector lymphocytes transendothelial migration but not SDF1-α induced chemotaxis.

(Ai) Adhesion, crawling and transendothelial migration (TEM) of human effector T cells pretreated with carrier control (DMSO) or 100 nM ZMP for 6 hours and subsequently washed before being perfused into the flow chamber. T lymphocyte adhesion and TEM were analyzed on Il-1β-activated HDBECs under shear flow for 10 min. (Aii) Nuclear lobe insertion kinetics of effector T cells during TEM. (Aiii) The nuclear passage duration from above to underneath the endothelial monolayer during TEM. Each dot represents a different T cell. (B) SDF-1α induced migration (30 min) of human effector T cells through 5 µm pore transwell filters. Cells were pretreated with carrier control (DMSO) or 100 nM ZMP for 6 hours and subsequently washed. The chemokine was added to the lower well at 60 nM. Data are mean ± SEM. The results shown are representative of two (Ai, Aii, Aiii) or three (B) independent experiments.

bioRxiv preprint doi: https://doi.org/10.1101/2020.06.23.167130; this version posted June 24, 2020. The copyright holder for this preprint (which was not certified by peer review) is the author/funder, who has granted bioRxiv a license to display the preprint in perpetuity. It is made available under aCC-BY-NC-ND 4.0 International license.

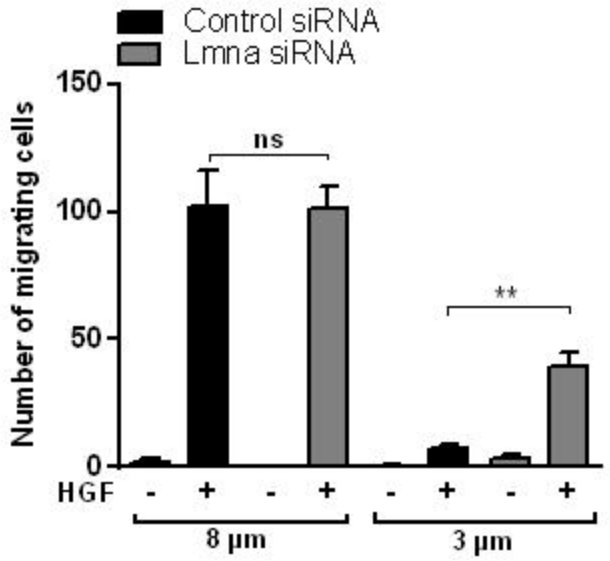

Figure S4. Lamin A/C deficiency increases B16 melanoma cells chemotaxis through rigid pores.

The migration of B16F10 cells, transfected with control or Lmna siRNA (72 hours before the experiment) towards HGF (50 ng/ml) measured through 8 or 3 µm pore transwell filters for 4 hours. Data are mean ± SEM. The results shown are representative of 2 independent experiments. **p = 0.0076.

bioRxiv preprint doi: https://doi.org/10.1101/2020.06.23.167130; this version posted June 24, 2020. The copyright holder for this preprint (which was not certified by peer review) is the author/funder, who has granted bioRxiv a license to display the preprint in perpetuity. It is made available under aCC-BY-NC-ND 4.0 International license.

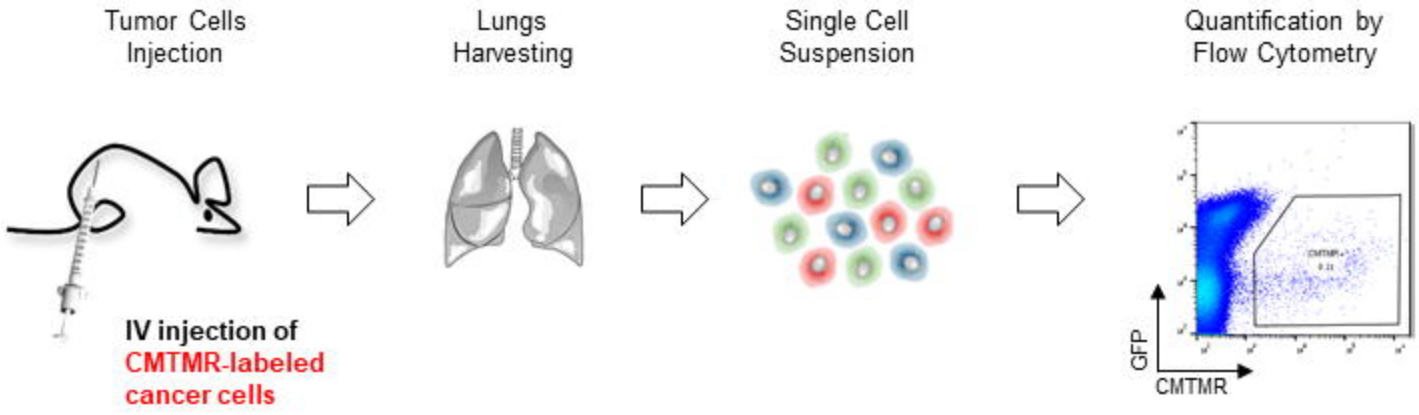

Figure S5. Quantification of cancer cells accumulation in lungs.
Scheme depicting the experimental pipeline necessary to quantify single cell accumulation in lungs of recipient mice. Cancer cells were labeled with CMTMR orange cell tracker for 30 min, washed and i.v. injected into recipient WT mice. After 3 hours, 3 or 7 days the mice were euthanized, their lungs harvested, minced and digested into single cell suspension and subsequently analyzed by flow cytometry.

bioRxiv preprint doi: https://doi.org/10.1101/2020.06.23.167130; this version posted June 24, 2020. The copyright holder for this preprint (which was not certified by peer review) is the author/funder, who has granted bioRxiv a license to display the preprint in perpetuity. It is made available under aCC-BY-NC-ND 4.0 International license.

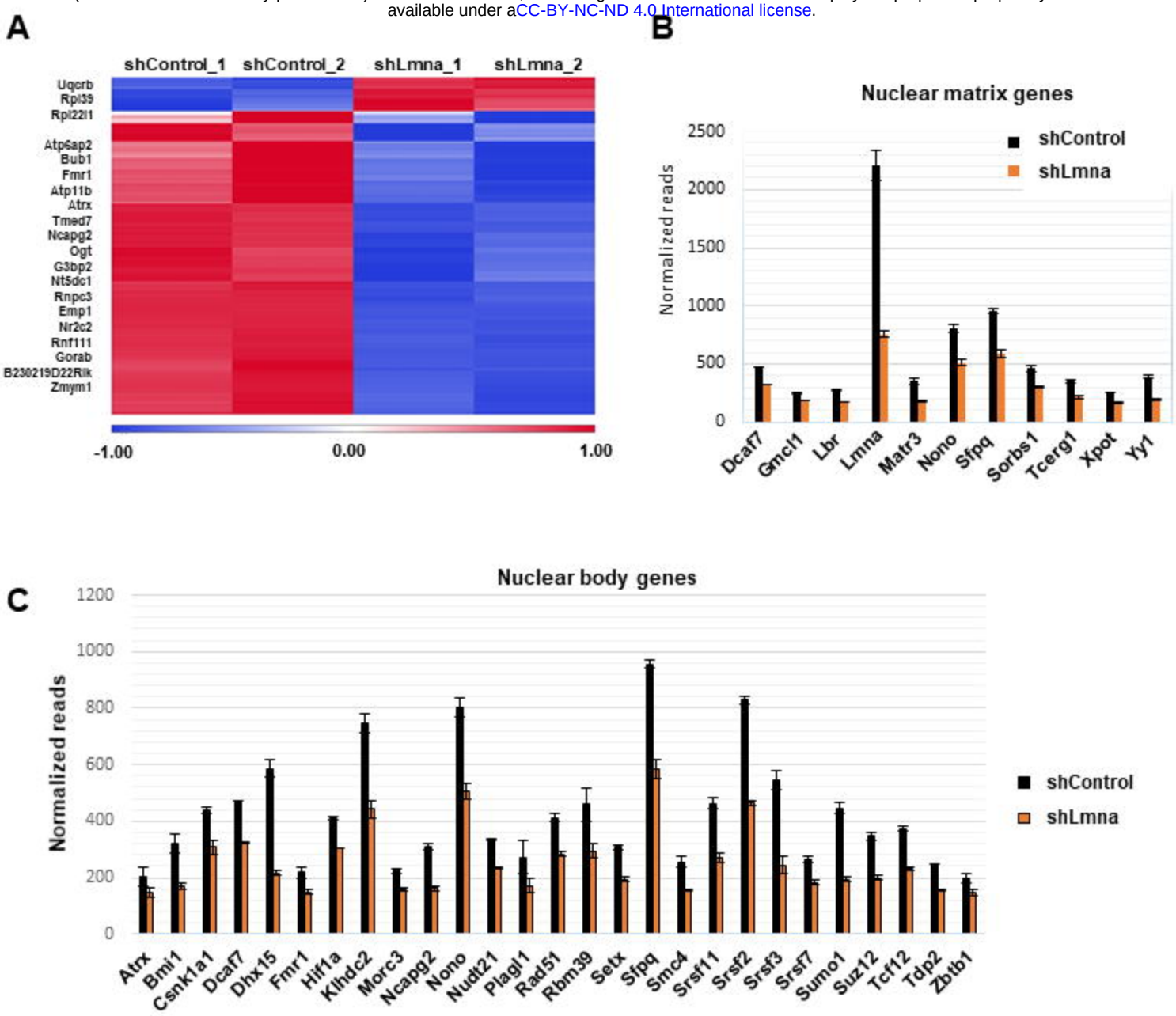

Figure S6. Lamin A/C downregulation alters gene transcription.
(A) Heatmap based on clustering of 300 differentially expressed genes. Red and blue bars represent positive and negative changes, respectively, and the intensity of the color represents the standardized log2 expression level. The top differentially expressed (DE) genes are shown on the left. The full list is available in Table S1. (B, C) Individual gene expression levels of genes belonging to the enriched gene ontology (GO) terms: nuclear matrix (B) and nuclear body (C), summarized in Fig. 6E.

bioRxiv preprint doi: https://doi.org/10.1101/2020.06.23.167130; this version posted June 24, 2020. The copyright holder for this preprint (which was not certified by peer review) is the author/funder, who has granted bioRxiv a license to display the preprint in perpetuity. It is made available under aCC-BY-NC-ND 4.0 International license.

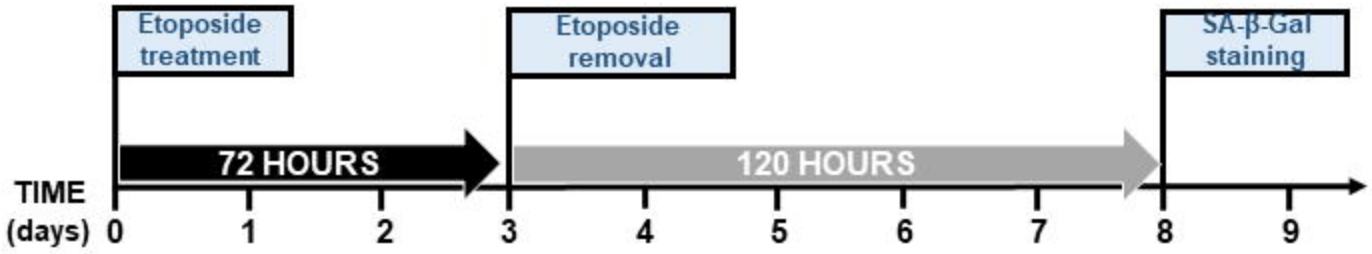

Figure S7. DNA damage-induced growth arrest and senescence of cancer cells induced by etoposide treatment in vitro.

Cancer cells were exposed to 5 μM etoposide for 72 hours. The compound was subsequently removed and the cells were cultured with regular growth medium for additional 120 hours. Cells were then fixed in 0.5% glutaraldehyde for 15 min and stained for senescence associated β-Galactosidase as described in Krizhanovsky et al., 2008.

bioRxiv preprint doi: https://doi.org/10.1101/2020.06.23.167130; this version posted June 24, 2020. The copyright holder for this preprint (which was not certified by peer review) is the author/funder, who has granted bioRxiv a license to display the preprint in perpetuity. It is made available under aCC-BY-NC-ND 4.0 International license.

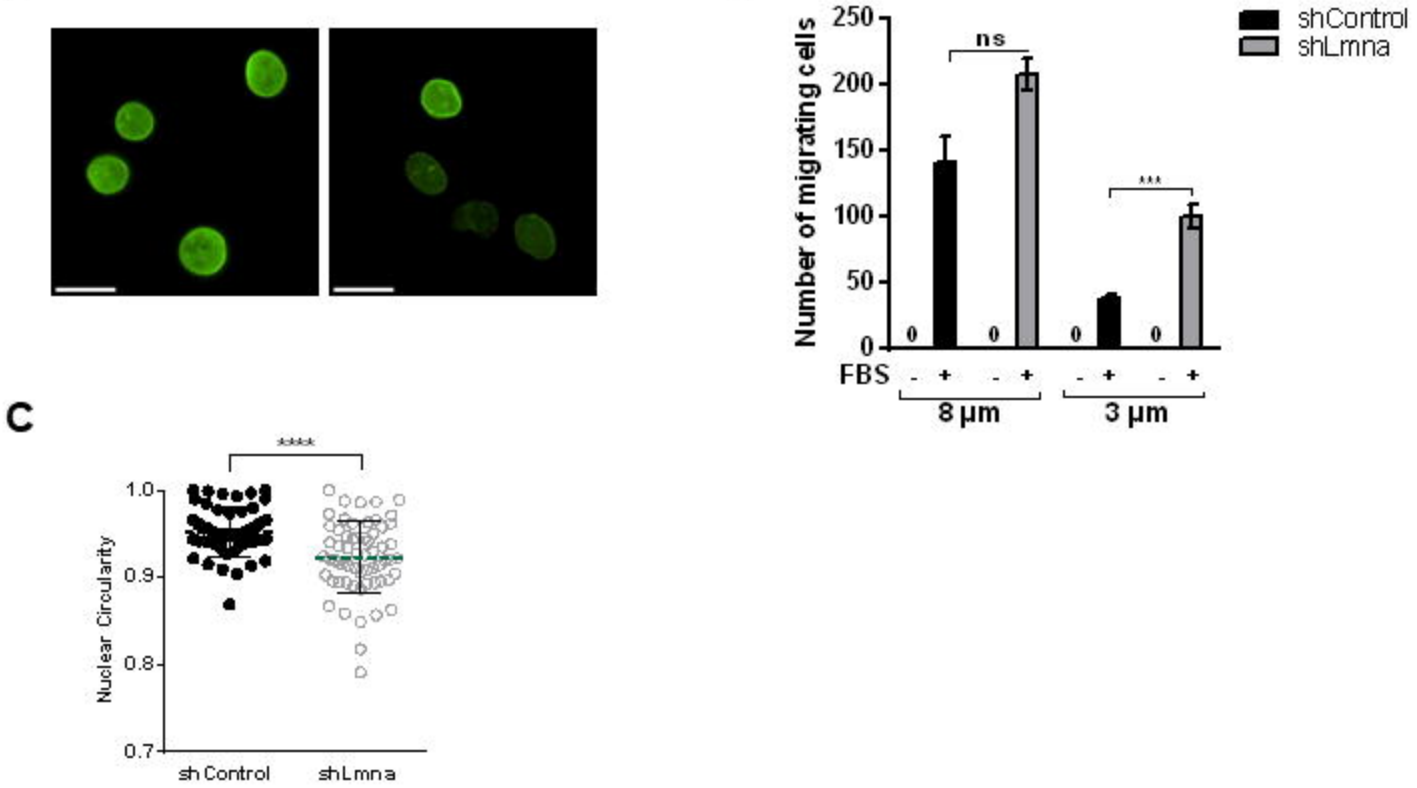

Figure S8. Downregulation of lamin A/C increases E0771 breast carcinoma cells squeezing through small rigid pores and alters nuclear shape

(A) Immunostaining of lamin A/C (green) in E0771 shControl and shLmna cells. Scale bar represents 20 µm. (B) Chemotactic migration of E0771 shControl and shLmna cells through 8 or 3 µm pores transwell filters in the presence (+) or absence (-) of DMEM containing 10% FBS for 24 hours. Values represent the mean ± SEM of five fields of view in each experimental group. Results shown are from a representative experiment of three. ***p = 0.0008. (C) Nuclear circularity of E0771 shControl and shLmna cells spread on a bEnd.3-derived basement membrane. ****p <0.0001

bioRxiv preprint doi: https://doi.org/10.1101/2020.06.23.167130; this version posted June 24, 2020. The copyright holder for this preprint (which was not certified by peer review) is the author/funder, who has granted bioRxiv a license to display the preprint in perpetuity. It is made available under aCC-BY-NC-ND 4.0 International license.

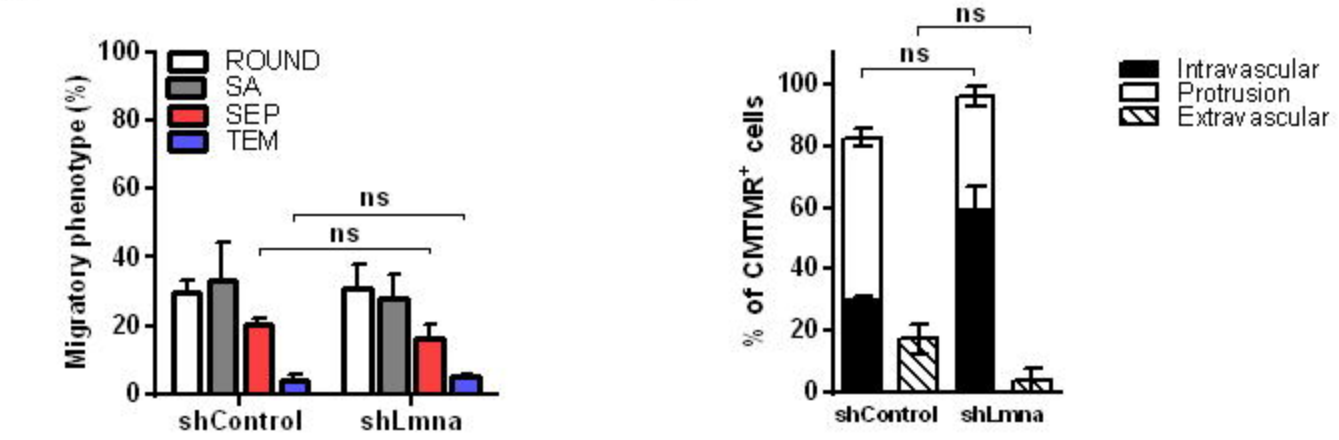

Figure S9. In vitro and in vivo breast carcinoma crossing of endothelial barriers is not enhanced by lamin A/C downregulation.

(A) Migratory phenotypes of E0771 breast carcinoma cells TEM. Distinct tumor cell categories (referred to as migratory phenotypes) taken from time lapse videomicroscopy segments of individual E0771 cells: round, spread above (SA), forming sub endothelial pseudopodia (SEP), and completing transendothelial migration (TEM). Values represent the mean ± SEM of three fields in each experimental group. (B) Percentage of E0771 shControl and shLmna cells in a volume of $5x10^9$ µm3 of the left lung lobe (3 days after injection). Values are mean ± SEM of 3 different lung's sections fields of view in each experimental group.

bioRxiv preprint doi: https://doi.org/10.1101/2020.06.23.167130; this version posted June 24, 2020. The copyright holder for this preprint (which was not certified by peer review) is the author/funder, who has granted bioRxiv a license to display the preprint in perpetuity. It is made available under aCC-BY-NC-ND 4.0 International license.

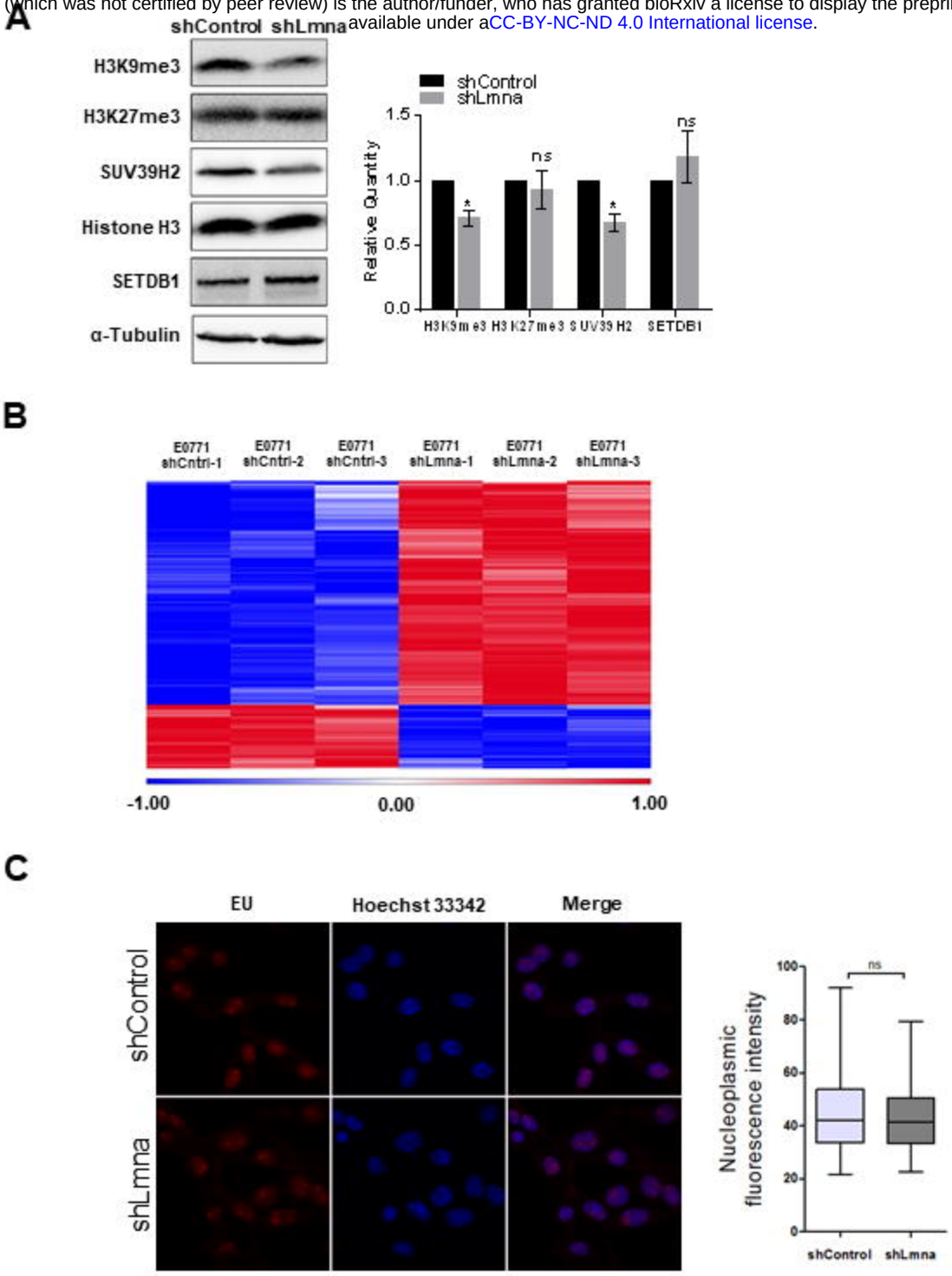

Figure S10. Lamin A/C downregulation reduces heterochromatin content and alters gene transcription.

(A) Equal protein amounts from E0771 shControl or shLmna cells, separated by SDS-PAGE and analyzed for the indicated proteins by Western blot analysis. The bar graph represents the mean levels of H3K9me3, H3K27me3 and SUV39H2 normalized to Histone H3 and of SETDB1 normalized to α-Tubulin ± SEM of at least four independent experiments. *$p < 0.05$. (B) Heatmap based on clustering of 290 differentially expressed genes. Red and blue bars represent positive and negative changes, respectively, and the intensity of the color represents the standardized log2 expression level. (C) Fluorescence microscopy imaging of 5-ethynyl uridine (EU) incorporation (red) and Hoechst 33342 (blue) in E0771 shControl and shLmna cells. Cells were grown with 1 mM EU for 1 h. The cells were fixed, permeabilized and treated with Alexa Fluor 594 azide. Nucleoplasmic fluorescence intensity of the EU staining was measured using ImageJ. Data from 3 independent experiments are shown in the boxplot.

bioRxiv preprint doi: https://doi.org/10.1101/2020.06.23.167130; this version posted June 24, 2020. The copyright holder for this preprint (which was not certified by peer review) is the author/funder, who has granted bioRxiv a license to display the preprint in perpetuity. It is made available under aCC-BY-NC-ND 4.0 International license.

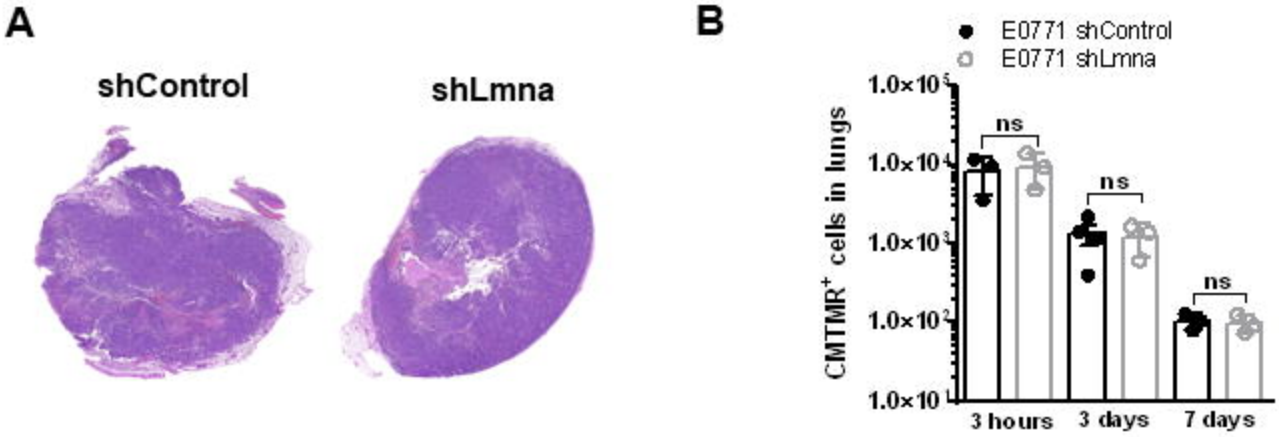

Figure S11. Primary breast tumor growth and cancer cells accumulation in lungs are insensitive to lamin A/C downregulation.

(A) Histology sections of breast primary tumors. A suspension of 10^4 E0771 (either shControl or shLmna expressing) cells in 50 µl of Matrigel® Matrix mixed with PBS (at 1:1 v/v) was inoculated in the mammary fat pad of recipient mice. 14 days later, animals were euthanized, tumors extracted, and fixed in 4% PFA. (B) Number of E0771 shControl and shLmna present in the lungs of recipient mice 3 hours, 3 and 7 days after i.v. injection. n = 3 for each experimental group. Data are mean ± SEM. The experiment shown is representative of three.